

The Low Redshift Lyman Alpha Forest in Cold Dark Matter Cosmologies

Romeel Davé and Lars Hernquist

Astronomy Department, University of California, Santa Cruz, CA 95064

Neal Katz

Astronomy Department, University of Massachusetts, Amherst, MA 01003

and

David H. Weinberg

Astronomy Department, Ohio State University, Columbus, OH 43210

ABSTRACT

We study the physical origin of the low-redshift Ly α forest in hydrodynamic simulations of four cosmological models, all variants of the cold dark matter scenario. Our most important conclusions are insensitive to the cosmological model, but they depend on our assumption that the UV background declines at low redshift in concert with the declining population of quasar sources. We find that the expansion of the universe drives rapid evolution of dN/dz (the number of absorbers per unit redshift above a specified equivalent width threshold) at $z \gtrsim 1.7$, but that at lower redshift the fading of the UV background counters the influence of expansion, leading to slow evolution of dN/dz . The draining of gas from low density regions into collapsed structures has a mild but not negligible effect on the evolution of dN/dz , especially for high equivalent width thresholds. At every redshift, weaker lines come primarily from moderate fluctuations of the diffuse, unshocked intergalactic medium (IGM), and stronger lines originate in shocked or radiatively cooled gas of higher overdensity. However, the neutral hydrogen column density associated with structures of fixed overdensity drops as the universe expands, so an absorber at $z = 0$ is dynamically analogous to an absorber that has column density 10 to 50 times higher at $z = 2 - 3$. In particular, the mildly overdense IGM fluctuations that dominate the Ly α forest opacity at $z > 2$ produce optically thin lines at $z < 1$, while the marginally saturated ($N_{\text{HI}} \sim 10^{14.5} \text{ cm}^{-2}$) lines at $z < 1$ typically arise in gas that is overdense by a factor of 20 – 100. We find no clear distinction between lines arising in “galaxy halos” and lines arising in larger scale structures; however, galaxies tend to lie near the dense regions of the IGM that are responsible for strong Ly α lines. The simulations provide a unified physical picture that accounts for the most distinctive observed properties of the low-redshift Ly α forest: (1) a sharp transition in the evolution of dN/dz at $z \sim 1.7$,

(2) stronger evolution for absorbers of higher equivalent width, (3) a correlation of increasing Ly α equivalent width with decreasing galaxy impact parameter that extends to $r_p \sim 500h^{-1}$ kpc, and (4) a tendency for stronger lines to arise in close proximity to galaxies while weaker lines trace more diffuse large scale structure.

Subject headings: galaxies: formation — large-scale structure of universe — quasars: absorption lines

1. Introduction

Ly α absorption by neutral hydrogen along the line of sight to distant quasars provides a sensitive probe of the cosmic distribution of diffuse gas over a wide range of redshifts (Bahcall & Salpeter 1965; Gunn & Peterson 1965; Scheuer 1965; Lynds 1971; Sargent et al. 1980). In recent years, the Keck telescope’s HIRES spectrograph (Vogt et al. 1994) has revolutionized the study of the Ly α “forest” at redshifts $z \sim 2 - 4.5$, yielding high-resolution spectra of spectacular precision (see, e.g., Hu et al. 1995; Lu et al. 1996; Kim et al. 1997, hereafter KHCS; Kirkman & Tytler 1998). At the same time, the UV spectroscopic capabilities of the Hubble Space Telescope (HST) have made it possible to study the Ly α forest from $z = 2$ down to $z = 0$. In particular, the HST Quasar Absorption Line Key Project team has used the Faint Object Spectrograph (FOS) to conduct a comprehensive census of low redshift Ly α lines, especially those with rest-frame equivalent width $W_r \geq 0.24\text{\AA}$, examining statistical quantities such as the distribution of equivalent widths, dN/dW_r , and the evolution of the number of lines per unit redshift above an equivalent width threshold, dN/dz (Bahcall et al. 1993, 1996; Jannuzi et al. 1998; Weymann et al. 1998, hereafter W98). Other groups have used the Goddard High Resolution Spectrograph (GHRS) to study weaker lines toward a smaller number of quasars (e.g., Morris et al. 1991; Stocke et al. 1995; Shull, Stocke & Penton 1996, hereafter SSP; Tripp, Lu, & Savage 1998, hereafter TLS). Future observations with the Space Telescope Imaging Spectrograph (STIS) and the Cosmic Origins Spectrograph (COS) should yield more extensive samples of weak low-redshift lines.

Concurrently with these observational developments, cosmological simulations that incorporate gravity, gas dynamics, radiative cooling, and photoionization have shown that theoretical models based on inflation and cold dark matter (CDM) can reproduce many of the observed properties of the high-redshift ($z > 2$) Ly α forest (e.g., Cen et al. 1994; Zhang, Anninos, & Norman 1995; Hernquist et al. 1996; Miralda-Escudé et al. 1996; Wadsley & Bond 1997; Bryan et al. 1998; Theuns et al. 1998ab). These theoretical models were originally introduced to account for the observed properties of galaxies, large scale structure, and cosmic microwave background anisotropies, so their success in explaining an entirely different class of observational phenomena provides important support for at least the broad features of the CDM scenario. The simulations lead to a physical picture in which most of the optically thin or marginally saturated lines at high redshift (those with neutral hydrogen column densities $N_{\text{HI}} \lesssim 10^{14.5}\text{cm}^{-2}$) arise in structures that

are only a few times the cosmic mean density and are therefore far from dynamical or thermal equilibrium. The physics of the diffuse intergalactic medium (IGM) that produces this low column density absorption is relatively simple, so this model of the high-redshift Ly α forest can be described with surprising accuracy by straightforward analytic or numerical approximations (e.g., Bi 1993; Bi, Ge, & Fang 1995; Mückel et al. 1996; Bi & Davidsen 1997; Hui, Gnedin, & Zhang 1997; Croft et al. 1998; Gnedin & Hui 1998; Weinberg, Katz, & Hernquist 1998b).

In this paper we use smoothed particle hydrodynamics (SPH) simulations to extend these numerical studies to $z = 0$, employing a newly developed parallel version (Davé, Dubinski, & Hernquist 1997a) of our simulation code TreeSPH (Hernquist & Katz 1989; Katz, Weinberg, & Hernquist 1996, hereafter KWH). We consider four variants of the CDM scenario (Peebles 1982; Blumenthal et al. 1984), two with $\Omega = 1$ and two with $\Omega = 0.4$. However, in this paper we focus on understanding the physics of the low- z forest rather than distinguishing between cosmological models. The Ly α forest is a promising new arena for cosmological tests, but these require a careful match between theoretical and observational analyses that is beyond the scope of the present study. We plan to pursue such comparisons at both low and high redshift in future work. At various points in the paper, we will compare our results to those of other numerical investigations of the low-redshift forest: Riediger, Petitjean, & Mückel (1998), who use a modified N-body method, and Theuns, Leonard, & Efstathiou (1998a), who use SPH simulations.

A surprise in the very first spectra of the low-redshift Ly α forest was the discovery of many more lines than expected from an extrapolation of high-redshift data (Bahcall et al. 1991; Morris et al. 1991). The implied change in the rate of evolution of the forest has now been precisely quantified by the Key Project team (W98). Adopting Sargent et al.’s (1980) parameterization of the evolution,

$$\frac{dN}{dz} = \left(\frac{dN}{dz} \right)_0 (1+z)^\gamma, \quad (1)$$

W98 find $\gamma = 0.26 \pm 0.22$ for a sample of nearly 500 lines with $W_r \geq 0.24\text{\AA}$ in the spectra of 62 quasars with $z \lesssim 1.5$. Ground-based studies imply much steeper evolution at $z > 2$ (e.g., Murdoch et al. 1986; Lu, Wolfe, & Turnshek 1991; Bechtold 1994), with the most recent results coming from the Keck/HIRES observations of KHCS, which yield $\gamma = 2.78 \pm 0.71$. Combining the HST and ground-based results implies a sharp break in the evolution of dN/dz at $z \sim 1.7$, which is further supported by W98’s analysis of the quasar UM 18 at $z = 1.89$. The break in evolution has led to the suggestion that there are two distinct populations of Ly α absorbers, one (perhaps associated with filaments and sheets) evolving rapidly and being dominant at high z , and the other (perhaps associated with galaxy halos) evolving slowly and being dominant at low z (e.g., Bahcall et al. 1993, 1996, who also discuss other possible causes for the break in dN/dz evolution).

The idea of an association between Ly α absorbers and gaseous halos of galaxies has a long history (e.g., Bahcall & Spitzer 1969). One important practical virtue of low- z forest studies is that follow-up observations can examine the relation between Ly α absorbers and the neighboring galaxies and large scale structure. For example, Lanzetta et al. (1995, hereafter LBTW) and Chen

et al. (1998, hereafter CLWB) have conducted deep imaging and spectroscopic surveys of galaxies in Key Project fields and find that galaxies with impact parameters $r_p < 160h^{-1}$ kpc almost always have an associated absorption line with $W_r \gtrsim 0.3\text{\AA}$, but that galaxies with $r_p > 160h^{-1}$ kpc almost never do (r_p is the projected distance from the galaxy to the quasar line of sight). They also find a trend of increasing Ly α equivalent width with decreasing galaxy impact parameter, a correlation that has been extended to larger r_p and smaller W_r by TLS (who add a cautionary discussion of selection biases that could artificially amplify the apparent trend). On this basis, LBTW and CLWB argue that most, and perhaps all Ly α absorbers with $W_r > 0.3\text{\AA}$ arise in extended gaseous envelopes surrounding galaxies, with typical radii $\sim 160h^{-1}$ kpc (weakly dependent on galaxy luminosity). However, numerous studies show that there are some Ly α absorbers with no luminous galaxy nearby (e.g., Morris et al. 1993; Bowen, Blades, & Pettini 1996; Le Brun, Bergeron, & Boissé 1996; van Gorkom et al. 1996; Le Brun & Bergeron 1998; TLS) even with impressively deep imaging (Rauch, Weymann, & Morris 1996). Comparison to wide-angle galaxy redshift surveys shows that some weak Ly α absorbers reside in large scale voids of the galaxy distribution (Stocke et al. 1995; SSP). Statistical analyses show that the low- z Ly α absorbers are not randomly distributed with respect to galaxies, but they also show that the cross-correlation between absorbers and galaxies is not as strong as the correlation of galaxies with themselves (Morris et al. 1993; Lanzetta, Webb, & Barcons 1998; TLS) and that the galaxy density around absorbers is lower than the galaxy density around galaxies (Grogin & Geller 1998). These analyses have led many of the above authors (and others as well) to suggest that low- z Ly α forest absorption is produced not by individual galaxies but by larger scale gaseous structures that the galaxies themselves reside in, with some tendency for weak absorbers to avoid high density regions and favor low density regions.

Given this observational background, we began our theoretical investigation of the low- z Ly α forest with several interlocking questions in mind. First, can the simulations account for the observed break in dN/dz evolution at $z \sim 1.7$, and if so, what is the mechanism causing the break? Second, are the physical structures that produce the Ly α forest the same at high and low redshift, or is there a transition from one population of absorbers to another? Third, if the low redshift picture is similar to the one at high redshifts, how do the simulations account for the apparent correlations between low- z absorbers and galaxies, and can they reconcile the somewhat contradictory evidence on absorber-galaxy associations supplied by different observational studies? We will argue below that the simulations provide a good account of the observed properties of the low- z forest, that the answer to the evolution question is fairly simple, and that the answers to the subsequent questions are clear but multi-faceted.

We describe our simulations and our method of creating and analyzing artificial spectra in §2. In §3 we compare dN/dz and dN/dW_r computed from our simulated spectra to the most recent analysis of Key Project data at low redshift (W98) and to an analysis of Keck HIRES spectra at high redshift (KHCS). In §4 we investigate the physical properties of the gas giving rise to Ly α absorption. In §5 we identify sites of galaxy formation in our simulations, and quantify

relationships between Ly α absorbers and galaxies. Finally, in §6 we summarize our conclusions on the nature of the Ly α forest at low redshifts.

2. Simulations and Artificial Spectra

We employ hydrodynamic simulations of four currently favored variants of the CDM scenario: a Lambda-dominated CDM model (LCDM) with $\Omega_\Lambda = 0.6$ (Liddle et al. 1996b), a tilted CDM model with a slope of $n = 0.8$ on large scales (TCDM; White et al. 1996), an open CDM model (OCDM) with $\Omega = 0.5$ (Liddle et al. 1996a), and a Cold + Hot Dark Matter model (CHDM) with two neutrino species totaling $\Omega_\nu = 0.2$ (Klypin, Nolthenius, & Primack 1997). The properties of the models are listed in Table 1; each is roughly consistent with COBE normalization, cluster normalization, and the baryon density $\Omega_b \approx 0.02h^{-2}$, as determined from recent measurements of the primordial deuterium abundance (Burles & Tytler 1998a,b) and as favored by the estimates of the mean opacity of the Ly α forest at high redshifts by Rauch et al. (1997b). The CHDM model has a slightly lower $\Omega_b h^2$ than the others.

The simulations were performed using Parallel TreeSPH (Davé et al. 1997a), a version of TreeSPH (Hernquist & Katz 1989; KWH) implemented on massively parallel supercomputers. We use 64^3 dark matter particles and 64^3 gas particles, with an additional 2×64^3 neutrino particles for the CHDM model, evolving within a periodic cube of $11.111h^{-1}$ comoving Mpc on a side and a gravitational softening length of $3h^{-1}$ comoving kpc (equivalent Plummer softening). We include a prescription for converting gas into stars (KWH). The starting redshift and the mass resolution for the dark matter and gas particles for each model are listed in Table 2. For the LCDM, TCDM, and OCDM simulations, the initial conditions are random realizations of a Gaussian field with the appropriate initial power spectrum; we use the same Fourier phases for each of the three models to minimize the effect of “cosmic variance” in a finite volume. The CHDM initial conditions were generated with routines provided by Klypin & Holtzman (1997) and thus have different random phases. Particles have individual timesteps according to their physical state; the total number of smallest timesteps to $z = 0$ and the total CPU time required are listed in Table 2. The calculations were run on Cray T3Es at the San Diego and Pittsburgh Supercomputing Centers, typically using 16 processors.

When computing radiative cooling and heating rates, we include the effects of photoionization by a spatially uniform UV background, determining ionic abundances by requiring a balance between creation and destruction rates for each ionic species (see KWH). We take the shape and intensity of the UV background spectrum J_ν from the calculations of Haardt & Madau (1996, hereafter HM), who assume that the UV background comes predominantly from quasar light reprocessed by the clumpy IGM. However, we use the results of a new version of this calculation (kindly provided by Piero Madau), which adopts Zheng et al.’s (1997) $\alpha = -1.8$ power law index for the mean intrinsic quasar spectrum instead of the earlier value of $\alpha = -1.5$. We will still refer to this J_ν as the HM spectrum.

While photoionization has little effect on the dynamical evolution of the gas in our simulations, it plays a crucial role in our Ly α forest calculations because it determines the neutral hydrogen fraction, and hence the Ly α opacity, in diffuse intergalactic gas. The parameter that controls the relation between neutral fraction and gas overdensity is the HI photoionization rate Γ_{HI} , the cross-section weighted integral of J_ν . Since the overall normalization of J_ν is not precisely known from either observation or theory, and since the relation between neutral fraction and overdensity also depends on the uncertain parameters Ω_b , h , and Ω , we follow the now-standard approach of renormalizing J_ν by a constant factor chosen so that artificial spectra from the simulation reproduce the observed value of the mean Ly α flux decrement (see, e.g., Miralda-Escudé et al. 1996). For each model, we choose this renormalization factor in order to match the mean decrement $\bar{D} = 0.32$ measured by Rauch et al. (1997b) at $z = 3$. We apply the *same* renormalization factor at all redshifts, so the evolution of Γ_{HI} (shown in Figure 4 below) is precisely that predicted by HM except for this overall multiplicative constant. The values of the J_ν renormalization factors are listed in Table 2, and they would not be significantly different if we chose to match the Rauch et al. (1997b) results at $z = 2$ instead of $z = 3$. In practice, we multiply the HI optical depths by the inverse of this factor instead of recalculating spectra with an increased J_ν ; the two procedures have the same effect on the highly photoionized gas that produces Ly α forest absorption at high redshifts. At low redshifts the procedure should also work, albeit not quite as well owing to a small number of features where collisional ionization cannot be ignored.

We extract artificial Ly α absorption spectra from the simulations using the TIPSYS package (Katz & Quinn 1995; see Hernquist et al. 1996 for details). We generate 400 spectra along randomly selected lines of sight (LOS) through the simulation volume at output redshifts of $z = 3, 2.5, 2, 1.75, 1.5, 1.25, 1, 0.75, 0.5, 0.25$ and 0. We sample the spectra with resolution $\Delta\lambda = 0.06\text{\AA}$, roughly corresponding to that of HIRES. We “fit a continuum” to each small spectral segment (equal in length to the size of the simulation box) by rescaling all flux values so that the highest flux pixel has transmission of unity — specifically, we multiply the flux values in all pixels by $\exp(\tau_{\text{min}})$, where τ_{min} is the optical depth of the highest flux pixel in the segment. This procedure removes $\sim 5\%$ of the flux at $z \sim 3$ (depending somewhat on cosmology), but for $z \lesssim 2$ the amount of flux removed is negligible. After rescaling the continuum, we add Gaussian random noise corresponding to a signal-to-noise ratio $S/N = 30$. Varying S/N over a reasonable range, e.g., between 20 and 50, does not have a significant effect on our conclusions. In the future, we will construct artificial spectra more closely matched to the properties of low- z data; for our current purposes, the level of similarity here is sufficient.

Figure 1 shows ten sample spectra from the LCDM simulation at $z = 3, 2, 1$ and 0, concatenated to give a wavelength coverage as indicated in the lower right corner. The same lines of sight are shown at each redshift, so to some extent individual features can be compared from one spectrum to another, though absorbing structures may move into or out of the line of sight over time. The most dramatic evolutionary effect is the paucity of absorption features at low redshift as compared to high redshift. The change would be smaller if we plotted the same

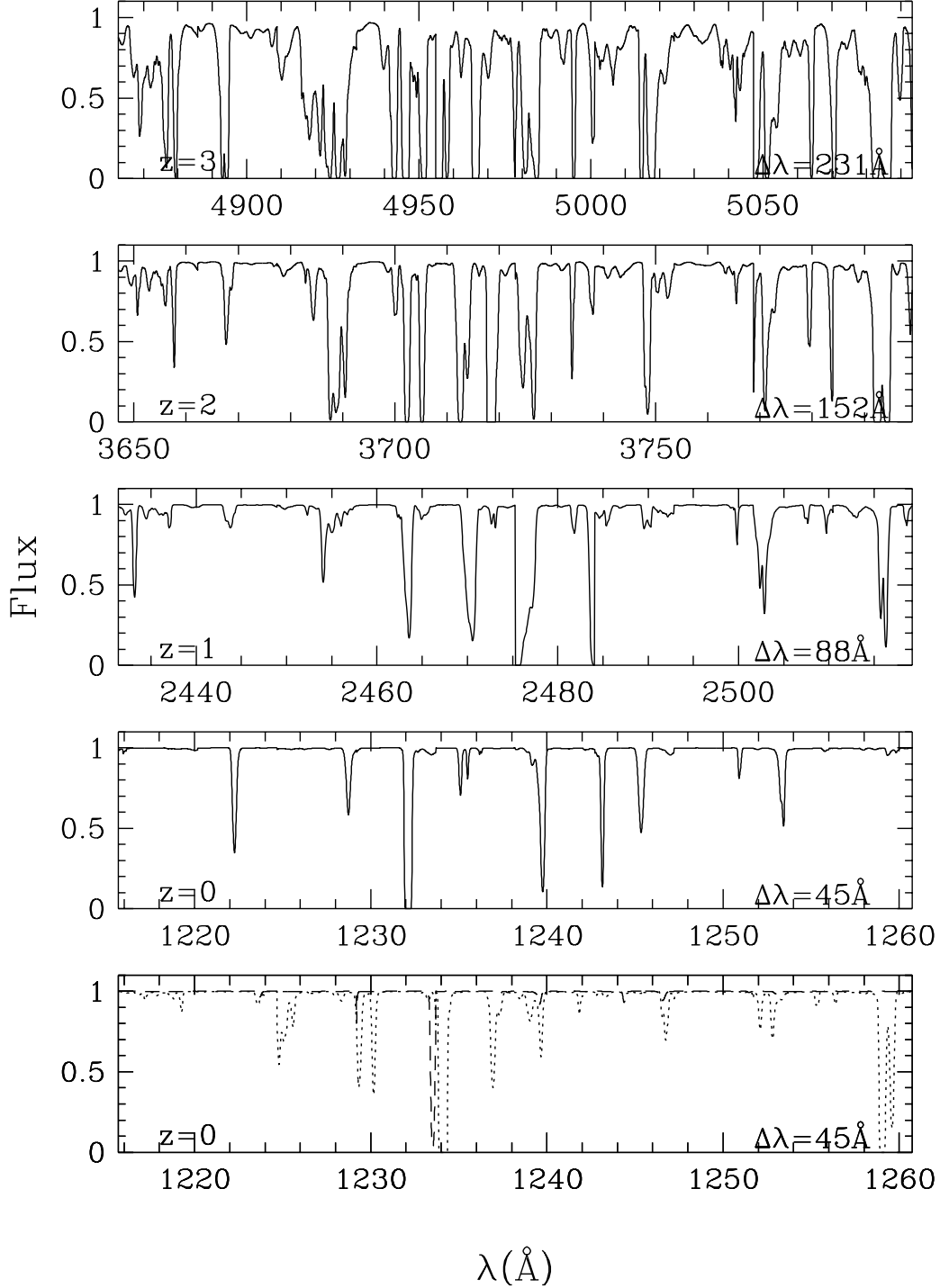


Fig. 1.— Ten artificial spectra at $z = 3, 2, 1$ and 0 from our LCDM simulation, concatenated. The same lines of sight are chosen at each redshift. The total wavelength coverage of the ten spectra is shown, in \AA , in the lower right. The strength and number of absorption features decrease to lower redshift. The bottom panel shows the $z = 0$ spectra for the structure evolution (dashed line) and J_ν evolution (dotted line) scenarios discussed in §3.4.

wavelength interval instead of the same comoving distance in each panel, but one can also see that individual features generally become weaker with time and that the mean flux decrement drops sharply between $z = 3$ and $z = 1$. We will discuss the cause of these changes and the significance of the bottom panel with the dashed and dotted lines in §3.4.

We fit Voigt profiles to each spectrum using the automated Voigt profile fitter AutoVP (Davé et al. 1997b), yielding a column density, a b -parameter (i.e., a Gaussian width of the optical depth profile), and a rest equivalent width for each line. Ly α absorbers are typically fully resolved at all redshifts in our artificial spectra, in contrast to currently available HST spectra. This represents a systematic difference that may affect the comparison of models to data at low redshift, although for most of the statistics we consider it is unlikely to dominate over other uncertainties.

Figure 2 presents a different view of absorption in the LCDM simulation, showing the HI column density in a 200 km s^{-1} thick slice at redshifts 3, 2, 1.5, 1, 0.5, and 0. The dimmest red level in the plot corresponds to a column density of $N_{\text{HI}} \approx 10^{13} \text{ cm}^{-2}$, which in turn corresponds to a line-center optical depth $\tau_c \approx 0.25$ for a Voigt-profile line with a b -parameter of 30 km s^{-1} . Orange corresponds to a column density of $10^{14} \text{ cm}^{-2} \lesssim N_{\text{HI}} \lesssim 10^{15} \text{ cm}^{-2}$ and yellow corresponds to $10^{15} \text{ cm}^{-2} \lesssim N_{\text{HI}} \lesssim 10^{16} \text{ cm}^{-2}$. The saturated, white level corresponds to $N_{\text{HI}} \gtrsim 10^{16} \text{ cm}^{-2}$, about a factor of 10 below the column density of a Lyman limit system. The positions of the compact, saturated dots typically correspond to the positions of galaxies (clumps of stars and cold, dense gas), although the luminous regions of the galaxies (and the cross-sections for producing damped Ly α absorption) would be virtually invisible on the scale of Figure 2.

From inspection of Figure 2, one can anticipate many of the conclusions that we will reach from more detailed analyses below. There is rapid evolution in the number of absorbers above a given threshold between $z = 3$ and $z = 1.5$, but the evolution is much slower between $z = 1.5$ and $z = 0$. The backbone of the structure traced by Ly α absorption does not change radically even over the full range $z = 3$ to $z = 0$; the evolution of the forest seems to correspond more to a shifting of contour levels rather than a transformation of the underlying structure. Finally, for any given choice of threshold, there will be a much closer correspondence between absorbing regions and galaxies at low redshift than there is at high redshift.

3. Evolution of dN/dz and dN/dW_r

3.1. Observations of dN/dz

At high redshift ($2 \lesssim z \lesssim 3$), KHCS find $\gamma = 2.78 \pm 0.71$ (where γ is defined in equation [1]) from HIRES spectra. Ground-based investigations prior to HIRES provided a somewhat confusing picture, some showing strong evolution ($\gamma \approx 2.8$; Lu et al. 1991) and some showing weak evolution ($\gamma \approx 1.7$; Bechtold 1994). We believe that the KHCS determination is more secure and most directly comparable with simulations, since the HIRES spectra are less subject to line blending

Fig. 2.— Column density of neutral hydrogen through a 200 km s^{-1} slice of the LCDM simulation volume at $z = 3, 2, 1.5, 1, 0.5,$ and 0 (left-to-right and top-to-bottom). Red corresponds to $10^{13} \text{ cm}^{-2} \lesssim N_{\text{HI}} \lesssim 10^{14} \text{ cm}^{-2}$, orange to a column density of $10^{14} \text{ cm}^{-2} \lesssim N_{\text{HI}} \lesssim 10^{15} \text{ cm}^{-2}$, yellow to $10^{15} \text{ cm}^{-2} \lesssim N_{\text{HI}} \lesssim 10^{16} \text{ cm}^{-2}$, and white to $N_{\text{HI}} \gtrsim 10^{16} \text{ cm}^{-2}$.

and make it possible to detect Ly α absorbers down to $W_r \sim 0.02\text{\AA}$. However, since the number of quasars currently observed with HIRES is small, the statistics are poor. The amplitude of dN/dz quoted by KHCS is for lines with $N_{\text{HI}} > 10^{13.77}\text{cm}^{-2}$, while our chosen rest equivalent width limit ($W_r > 0.24\text{\AA}$) corresponds (for typical b -parameters) to $N_{\text{HI}} \gtrsim 10^{13.9}\text{cm}^{-2}$; we have therefore applied a small correction to KHCS’s value of $(dN/dz)_0$ based on the overall column density distribution taken from their paper.

For $z \lesssim 1.5$, W98 have published the most complete analysis of evolution in the Key Project sample, obtaining $\gamma = 0.26 \pm 0.22$ and $(dN/dz)_0 = 32.7 \pm 4.2$. The sample we use for comparison is their uniform detection limit sample of lines with $W_r > 0.24\text{\AA}$ (including Ly α systems with associated metal lines), although the results from other samples are not markedly different. W98 do find a trend of more rapid evolution of stronger lines, an issue we will address in §3.5 below.

3.2. Modeling Uncertainties

The size of our simulation volume introduces significant uncertainties when comparing the models with the data. By $z = 1$, all our models have nonlinear density fluctuations on the scale of the box length. Hence, the artificial spectra at low- z are not necessarily a representative sample for that cosmology, since the large scale power absent in these small volume simulations could have a substantial effect on the density fluctuations at all scales. We do not yet have the ability to gauge this systematic uncertainty, as to do so would require simulating a larger volume than is currently computationally feasible. Nevertheless, we can examine some general trends that should be valid despite these limitations. Furthermore, we have explicitly minimized the impact of finite volume statistical fluctuations on comparisons among the Λ CDM, TCDM, and LCDM models by using the same initial phases and lines of sight in each simulation. The differences between these results should therefore reflect inherent differences among the models (with the caveat that differences in power on scales larger than the box size could impact smaller scales).

Another uncertainty arises from the finite resolution of these simulations. As Wadsley & Bond (1997) have noted, the number of intermediate density Ly α forest absorbers ($N_{\text{HI}} \gtrsim 10^{15.5}\text{cm}^{-2}$, or $W_r \gtrsim 0.5\text{\AA}$) at $z = 3$ is somewhat sensitive to numerical resolution, since these systems are often associated with virialized “mini-halos” (Ikeuchi 1986; Rees 1986) of small mass and spatial extent. At high redshift, these mini-halos probably contribute no more than half of the total number of absorbers above $W_r \sim 0.6\text{\AA}$ (Gardner et al. 1997a) and a much smaller fraction of the number above $W_r \sim 0.24\text{\AA}$. However, as we shall show in §4.1, a given equivalent width absorber corresponds to higher overdensity gas at lower redshift, meaning that the fractional contribution of mini-halos above $W_r \sim 0.24$ will increase at lower redshifts. If our simulations are unable to resolve these objects, it is possible that we are increasingly underestimating the total number of lines at lower redshifts. We will eventually conduct higher resolution simulations to examine this possibility in more detail. Recently Theuns et al. (1998b) and Bryan et al. (1998) have examined the sensitivity of *high* redshift Ly α forest predictions to the numerical resolution of hydrodynamic

simulations. Both groups find that the predicted column density distribution is reasonably robust to changes in resolution but that convergence of the b -parameter distribution requires very high resolution.

In addition to these numerical uncertainties, there are sizeable uncertainties in the UV background spectrum. We take the evolution of J_ν directly from HM, who calculated the intensity based solely on the observed quasar population at various epochs. However, there could be an important contribution to the metagalactic flux from other sources such as starburst galaxies and AGNs, especially as the quasar population declines. This does not necessarily imply that J_ν will be higher than HM predict, since corrections for dust and intervening HI absorption can be large and are uncertain (Devriendt et al. 1998). Furthermore, the intrinsic spectral energy distribution of quasars, assumed by HM to follow a power law with slope $\alpha = -1.8$, is not well determined, and it could in principle vary with redshift, particularly through a correlation between luminosity and its slope (Korista, Baldwin, & Ferland 1998). These variations would be directly reflected in the number of HI lines observed. We consider this issue further in §3.3.

In sum, we expect the simulation predictions of the Ly α forest to be fairly reliable at high redshift but less so at low redshift, where the effects of the finite simulation volume and finite resolution are more significant, the UV background history is more uncertain, and the noise and resolution properties of our artificial spectra are less closely matched to current observational data (see §2). We are not yet in a position to gauge the magnitude of some of these uncertainties, especially those related to purely numerical effects. We will therefore not attempt to rule out any of the cosmological models that we consider on the basis of low- z Ly α forest data. Instead, we focus in this paper on the physical processes that give rise to Ly α forest absorption at various redshifts, with particular attention to those trends that are independent of the details of the cosmological model.

3.3. The Evolution of dN/dz in Various Cosmologies

Figure 3 shows the redshift evolution of dN/dz in our four cosmologies from $z = 3$ to $z = 0$. For the LCDM model, we show 1σ statistical uncertainties computed by taking the dispersion among 10 subsamples of 40 random LOS and dividing by $\sqrt{N - 1} = 3$. Statistical errors for the other models are comparable. Note, however, that these error bars do not incorporate systematic uncertainties from numerical limitations or mismatch between observational and theoretical analysis procedures, and they underestimate the true statistical error because we have only a single realization of structure for each cosmological model. Table 3 shows γ inferred from the observations and the simulations in various redshift intervals. We have not listed uncertainties for γ from the simulations, since at high redshift they are smaller than the uncertainties from KHCS, and at low redshift they are likely to be dominated by unquantified systematic errors.

For $2 \lesssim z \lesssim 3$, the LCDM and OCDM models are in good agreement with the data, while the

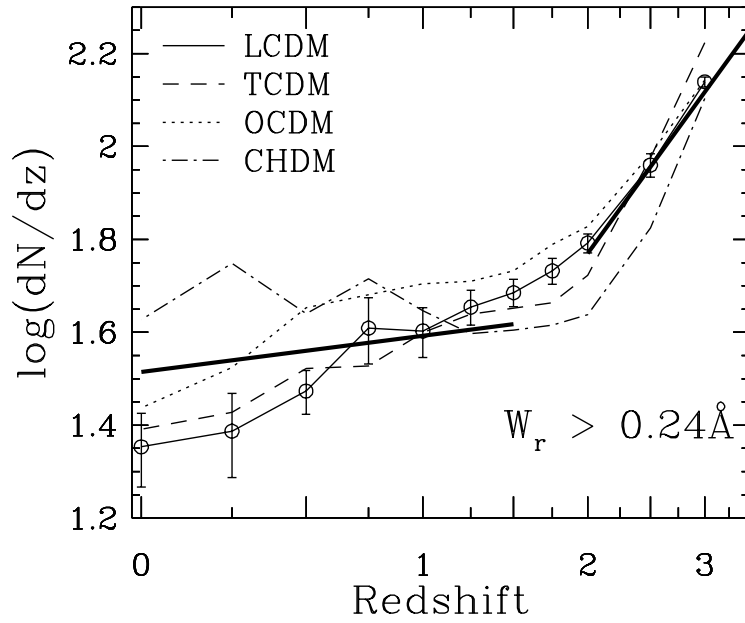


Fig. 3.— Evolution of dN/dz in various cosmologies. The thick solid line above $z \geq 2$ is from the observations of KHCS, while the thick solid line at $z \leq 1.5$ is a fit from W98. All cosmologies show a change in evolution of dN/dz after $z \sim 2$. The horizontal axis scale in this and subsequent evolution figures is linear in $\log(1+z)$, so that power laws in $(1+z)$ appear as straight lines.

TCDM and CHDM models show steeper evolution, with values of γ that lie outside the formal 1σ error of the KHCS estimate. The number of lines with $W_r > 0.24\text{\AA}$ in the CHDM model at $z = 2$ is significantly lower than observed, a failing that reflects the paucity of small-scale structure at early epochs in a CHDM universe. The intensity of the ionizing background has been normalized in each model to reproduce the Rauch et al. (1997b) measurement of the mean Ly α flux decrement at $z = 3$, so the value of dN/dz cannot be altered by changing J_ν without spoiling the agreement with other data. Detailed comparisons of these models to high-redshift data with a more careful treatment of systematic uncertainties will be presented elsewhere.

At $z \sim 2$, the rate of evolution of dN/dz starts to decrease in all the models. The history of structure formation is very different from one model to another, and the similarity of the dN/dz curves is an important clue that the break in dN/dz evolution is not caused primarily by the gravitational growth of structure (see §3.4 below). For LCDM, TCDM, and OCDM, dN/dz continues to drop with redshift down to $z = 0$, while for CHDM the slope is consistent with zero below $z \sim 1.5$. The spectral resolution of our artificial spectra is considerably higher than that typical of FOS spectra; blending caused by poorer resolution tends to raise the number of lines above $W_r > 0.24\text{\AA}$, but the overall rate of evolution does not change significantly. At face value, the CHDM model is in better agreement with the low redshift data than LCDM, TCDM or OCDM. However, uncertainties in J_ν at low redshift are much too large to allow any meaningful discrimination between cosmologies based on dN/dz evolution, even disregarding the other uncertainties noted in §3.2.

To gauge the sensitivity of γ to the evolution of J_ν , we determine the evolution of the photoionization rate Γ_{HI} for the LCDM simulation that would be required to produce perfect agreement with the observed evolution of dN/dz at $z \lesssim 1.5$. We obtain an initial guess for the required evolution of Γ_{HI} by simply multiplying the HM value of Γ_{HI} at redshifts $z = 1.5, 1, 0.5$, and 0 by the ratio of the observed dN/dz and dN/dz from the LCDM model with the original HM Γ_{HI} . This first correction brings dN/dz within 10% of the observed value. Minor adjustments then produce the evolution of Γ_{HI} shown in Figure 4. The solid line is the evolution of Γ_{HI} directly from HM, while the dashed line shows the evolution of Γ_{HI} that would yield exact agreement with the evolution of dN/dz from W98, for the LCDM model. The differences are not large — at most 50% at $z = 0$ — and other cosmologies would have differences that are typically smaller than that of the LCDM model (cf. Figure 3). An independent theoretical estimate of the evolution of Γ_{HI} from Fardal, Giroux, & Shull (1998, their Q1 model) is shown as the dotted line. The agreement between the HM and Fardal et al. (1998, hereafter FGS) models is impressively good, but both of them rest on the assumption that the UV background is produced entirely by quasar sources, and both of them rely on Pei’s (1995) estimate of the evolution of the quasar luminosity function.

Vogel et al. (1995) have used H α surface brightness measurements of a local HI cloud to place an upper limit on Γ_{HI} at $z = 0$, which is shown by the triangle in Figure 4. The circle at $z = 0.5$ shows Kulkarni & Fall’s (1993) estimate of J_ν from the proximity effect (converted using $\Gamma_{\text{HI}} = 2.64 \times 10^9 J_\nu$ in cgs units; see FGS). The uncertainties in these measurements are much

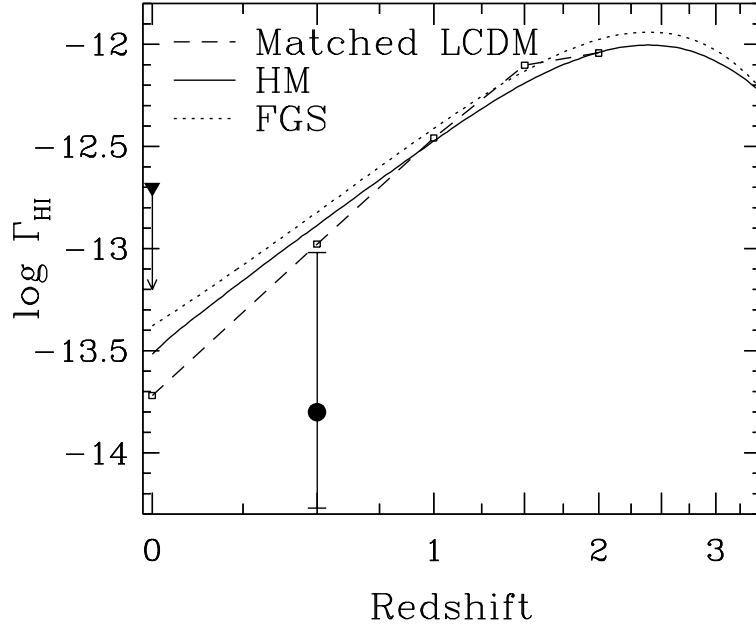


Fig. 4.— The evolution of Γ_{HI} from HM (solid line) and FGS (dotted line), and the evolution of Γ_{HI} required to force agreement between the LCDM model and the observed low- z dN/dz (dashed line). The differences are small compared to the uncertainties in observational estimates of Γ_{HI} from the proximity effect (Kulkarni & Fall 1993, solid circle) and from $\text{H}\alpha$ flux measurements (Vogel et al. 1995, solid triangle).

larger than the variation in Γ_{HI} required to reconcile the LCDM model with the Key Project data. Much more precise observational determinations of Γ_{HI} would be needed to directly test cosmological models using the value of dN/dz at low redshift.

A more promising route to testing cosmological models is to choose the value of Γ_{HI} at each redshift in order to match one observational datum, then use other statistical properties of the Ly α forest as tests of the model. One option is to adopt dN/dz as the “normalizing” observation – in this case we would use the values of Γ_{HI} shown in Figure 4 for the LCDM model. An alternative normalizing datum is the mean flux decrement \bar{D} , which has the advantages of not depending on a line identification algorithm and of being independent of spectral resolution. Figure 5 shows the evolution of \bar{D} in our simulations, with data points at $z = 2.29$ and $z = 3.02$ from Rauch et al. (1997b). As discussed in §2, we adjust the intensity of J_ν (with the HM shape) in each model to obtain agreement with the observed \bar{D} at $z = 3$. The subsequent predicted evolution of \bar{D} relies on the HM UV background history. With this history, all of the models continue to match the Rauch et al. (1997b) data at $z = 2.29$. We do not know of any determinations of \bar{D} from HST spectra at low redshift, although it should be straightforward in principle to estimate from existing data. The trends in the evolution of \bar{D} are similar to the trends in the evolution of dN/dz , as one would expect.

3.4. The Cause of the Break in dN/dz Evolution

The primary driver of evolution in dN/dz at high redshift is the expansion of the universe (Hernquist et al. 1996; Miralda-Escudé et al. 1996; Bi & Davidsen 1997). The *physical* density associated with a given *overdensity* drops as the universe expands, and as a result the neutral hydrogen fraction, which is proportional to the recombination rate, also drops. The neutral column density of any structure that is expanding with residual Hubble flow drops because of the reduced neutral fraction and because of expansion along directions perpendicular to the line of sight. At any redshift there are fewer high column density systems than low column density systems, so as the expansion of the universe drives the column density of each system down, the number of lines above any given threshold column density declines.

It is clear from observations and from our simulations that the evolution of dN/dz is much slower at low redshift, with a rather sharp transition in the evolution rate occurring at $z \sim 1.7$. We consider two physical processes that could influence dN/dz evolution in addition to the Hubble expansion effects described above:

1. “Structure evolution”: gravitational growth of structure drives gas from low density regions into filaments and sheets and from filaments and sheets into collapsed objects, so that the physical structures producing Ly α forest absorption are fundamentally different at low and high redshifts.

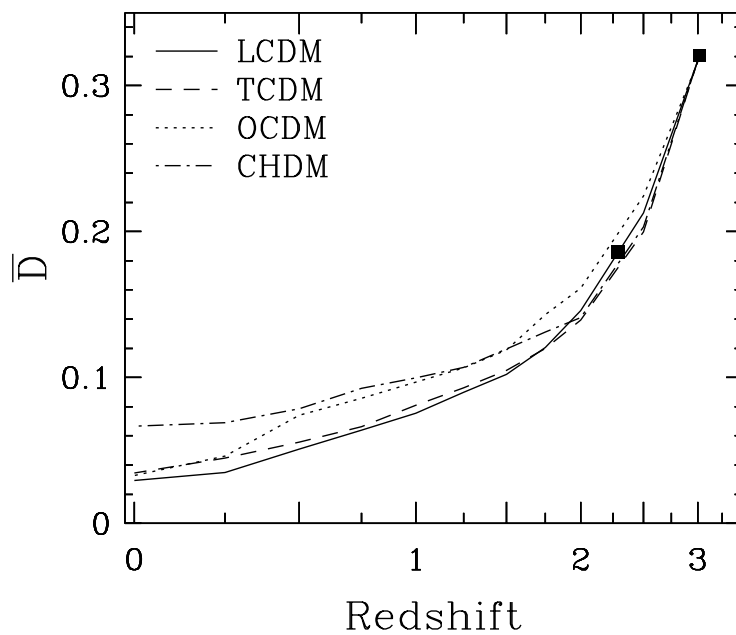


Fig. 5.— Evolution of the mean Ly α flux decrement, $\bar{D} \equiv \langle 1 - e^{-\tau} \rangle$. Filled squares are \bar{D} from sample of Keck/HIRES spectra analyzed by Rauch et al. (1997b). All models agree well with \bar{D} evolution for $z = 2 - 3$.

2. “ J_ν evolution”: the intensity of the UV background drops at $z < 2$ because of the declining quasar population, so that the lower recombination rate at low redshifts is countered by a lower photoionization rate.

Clearly both of these effects must operate in a complete model, but we would like to know whether one predominates in changing the evolution rate. To investigate this question, we consider idealized treatments of the LCDM simulation that isolate the two effects. The “structure evolution scenario” is represented by a model in which the intensity of the HM ionizing background is held fixed at its value at $z = 2$ and only the distribution of matter is varied from $z = 3$ to $z = 0$. The “ J_ν evolution scenario” is represented by a model in which the gas distribution is held fixed in comoving coordinates at its $z = 2$ distribution but the ionizing background is varied with redshift as prescribed by HM. Hubble expansion is included in both scenarios. In a pure J_ν evolution scenario, the changes in Figure 2 would be exactly equivalent to a shift in the color map from one redshift to another. Figure 6 presents the evolution of the projected column density in this 200 km s^{-1} slice (the same one as Figure 2) in the form of a contour plot. Contours are spaced by factors of 10 in column density, with the heavy contours corresponding to column densities of 10^{11} , 10^{14} , and 10^{17} cm^{-2} . A factor of ten change in J_ν at fixed redshift would correspond to a shift of one contour level in this plot, while for a fixed J_ν and fixed comoving gas distribution, the column densities would be proportional to $(1 + z)^5$ (see discussion below).

The bottom panel of Figure 1 shows artificial spectra at $z = 0$ along the same ten lines of sight shown in the panel above, from the structure evolution scenario (dashed line) and the J_ν evolution scenario (dotted line). Comparing to the true $z = 0$ spectrum, it is evident that, while neither idealization exactly reproduces the full evolution, the J_ν evolution scenario comes much closer. Figure 7 quantifies this impression in terms of dN/dz . The solid line shows the true dN/dz evolution of the LCDM simulation, reproduced from Figure 3, and the heavy dashed and dotted lines show dN/dz from the structure and J_ν evolution scenarios, respectively. The structure evolution scenario predicts a redshift evolution with no apparent break; the power law from $z \gtrsim 2$ continues smoothly down to lower redshifts, with $\gamma \approx 2.5$ from $z = 2$ to $z = 0$. Conversely, the J_ν evolution scenario predicts a distinct break beginning around $z \sim 2$. We conclude that the break in dN/dz evolution in the simulations (and, by implication, in the observations) is caused primarily by the decline of the UV background at low redshift. Coincidentally, the evolution of the HM background is just enough to roughly cancel the effects of Hubble expansion, yielding $\gamma \approx 0$. A similar analysis for the TCDM or CHDM models yields the same general conclusion.

Since the dotted and solid curves in Figure 7 do not agree perfectly, it appears that structure evolution does have some influence on dN/dz evolution, as one would expect. The effect of gravitational growth of the underlying structure is to *reduce* the number of absorbers observed above an equivalent width threshold, as matter empties from large scale structure into collapsed objects that have smaller cross-sections of absorbing gas.

The J_ν evolution scenario for dN/dz can be approximated analytically. The simplifying

Fig. 6.— Neutral hydrogen column density in the same 200 km s^{-1} thick slice as that shown in Figure 2. The contours are spaced by factors of 10 in column density. The heavy contours correspond to column densities of 10^{11} , 10^{14} , and 10^{17} cm^{-2} .

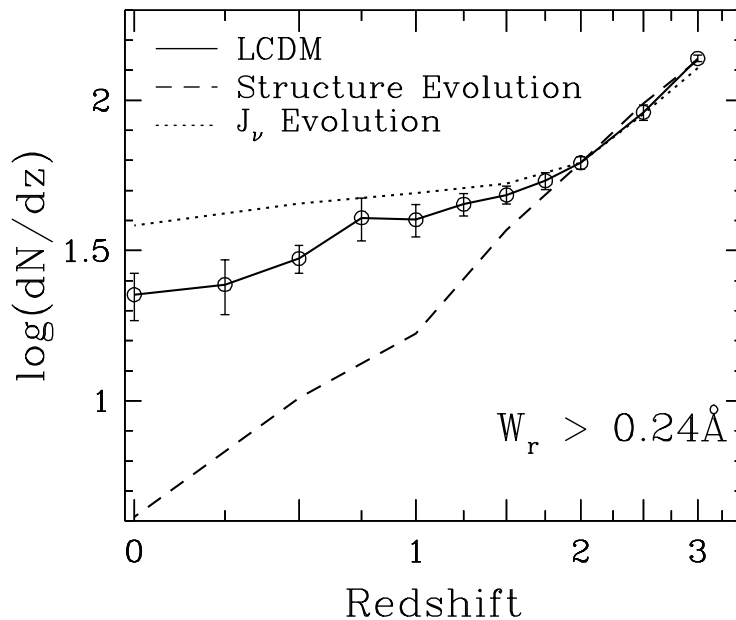


Fig. 7.— dN/dz from varying only structure or only J_ν . For $2 \lesssim z \lesssim 3$, the dominant effect is Hubble expansion, as J_ν and structure both remain roughly constant. For $z \lesssim 2$, the structure evolution (dashed line) and J_ν evolution (dotted line) models diverge rapidly, demonstrating that the observed break is caused predominantly by changes in J_ν . However, dN/dz from the J_ν evolution model evolves more slowly than that from the full LCDM simulation (solid line), indicating that structure formation plays a non-negligible role.

assumption of this scenario is that the gas distribution remains fixed in comoving coordinates, so that the gas density at a comoving position drops as $(1+z)^3$ in proportion to the mean density of the universe. If we ignore collisional ionization, then the neutral hydrogen fraction is proportional to the recombination rate divided by the photoionization rate, and hence to $(1+z)^3\Gamma_{\text{HI}}^{-1}(z)$. The neutral hydrogen column density of a given line is equal to the total column density times the neutral fraction and is therefore proportional to $(1+z)^5\Gamma_{\text{HI}}^{-1}(z)$. The additional factor of $(1+z)^2$ accounts for the decrease in total column density caused by the expansion of the absorber along the two dimensions perpendicular to the line of sight. Unless the photoionization rate falls faster than $(1+z)^5$, the neutral column density of every absorber falls, and systems that were once above a column density threshold drop below it as the universe expands, driving dN/dz down. A compensating effect is that the redshift interval Δz that corresponds to a comoving distance interval ΔX is proportional to the Hubble parameter $H(z)$. Therefore, for a fixed comoving structure, the number of lines per unit redshift is also proportional to $H^{-1}(z)$.

To obtain a quantitative prediction from this approximation, suppose that at a fiducial redshift z_f the distribution of HI column densities is a power law,

$$f(N_{\text{HI}}) \equiv \frac{dN}{dN_{\text{HI}}} \propto N_{\text{HI}}^{-\beta}. \quad (2)$$

Observations imply $\beta \approx 1.5 - 1.7$ at $z \sim 2 - 3$ (e.g., Petitjean et al. 1993; KHCS), and our numerical simulations yield column density distributions that are reasonably close to power laws with similar values of β . The number of lines above a limiting column density is the integral of this distribution, $F(N_{\text{HI,lim}}) \propto N_{\text{HI,lim}}^{1-\beta}$. To determine the number of lines above $N_{\text{HI,lim}}$ at some other redshift z , we can count the lines at redshift z_f above a different limiting column density

$$N'_{\text{HI,lim}} = N_{\text{HI,lim}} \left(\frac{1+z_f}{1+z} \right)^5 \frac{\Gamma_{\text{HI}}(z)}{\Gamma_{\text{HI}}(z_f)}. \quad (3)$$

Combining this shift in threshold with $F(N_{\text{HI,lim}})$ and the comoving distance to redshift conversion, we obtain

$$\left(\frac{dN}{dz} \right)_{>W_{r,\text{lim}}} = C \left[(1+z)^5 \Gamma_{\text{HI}}^{-1}(z) \right]^{\beta-1} H^{-1}(z), \quad (4)$$

where C is a constant chosen to match dN/dz at $z = z_f$.

In equation (4) we implicitly assume that an equivalent width threshold can be identified with a column density threshold. This identification is exact in the case of optically thin lines, and it is a reasonable approximation for mildly saturated lines because the distribution of column densities is much broader than the distribution of b -parameters. It is clear from equation (4) that dN/dz should drop rapidly with redshift if Γ_{HI} is constant but that a declining $\Gamma_{\text{HI}}(z)$ can cancel the effects of Hubble expansion on dN/dz . This analytic approach provides an approximate match to the numerical results for fixed comoving structure, demonstrating the simplicity of the underlying evolution mechanism: at different redshifts, a different column density or equivalent width threshold selects a different subset of the line population. However, the analytic description

implicitly assumes that Voigt-profile decomposition measures correct neutral column densities for a discrete set of absorbing structures and that the distribution of these column densities is well described by a single power law; detailed analysis of the simulations often undermines both of these assumptions.

Our conclusion that the drop in the UV background is the primary cause of the break in dN/dz is the same as that reached by Theuns et al. (1998a) on the basis of similar SPH simulations. We believe that this is also the explanation for the change in evolution rate found by Riediger et al. (1998) in their pseudo-hydro N-body simulations, although Riediger et al. do not emphasize this interpretation.

3.5. The Evolution of dN/dW_r

Observations show that the distribution of rest equivalent widths W_r of Ly α absorbers is roughly exponential, i.e.

$$\frac{dN}{dW_r} \propto e^{-W_r/W_r^*}. \quad (5)$$

W_r^* has been determined for high- z Ly α absorbers by several pre-HIRES studies, ranging from $W_r^* \approx 0.36\text{\AA}$ (Sargent et al. 1980) to $W_r^* \approx 0.28\text{\AA}$ (Murdoch et al. 1986) to $W_r^* \approx 0.16\text{\AA}$ (Carswell et al. 1984). The differences are likely attributable to spectral resolution and blending effects (Carswell et al. 1984). HIRES studies have focused on the distributions of N_{HI} and b , but given the good agreement of these distributions between simulations and data at high redshift (e.g., Zhang et al. 1995; Davé et al. 1997b), we expect that our high-redshift determinations of W_r^* will be in good agreement with the observations as well. Low- z Ly α absorbers are observed to have somewhat lower W_r^* , although it is unclear whether this difference reflects a change in the intrinsic properties of absorbers or biases introduced by poorer resolution at low redshift and line blending at high redshift (Lu et al. 1991; Bahcall et al. 1996).

Figure 8 shows the distribution of equivalent widths at $z = 3, 2, 1$, and 0 from our LCDM simulation. The lines show the best fit to equation (5), and the corresponding values for W_r^* are indicated in the legend. The distributions are truncated at high W_r when the number of absorbers in a bin of width 0.04\AA is zero.

The equivalent width distributions from our simulations are reasonably well described by exponentials at all redshifts. W_r^* decreases steadily and significantly with redshift, from $\approx 0.17\text{\AA}$ at $z = 3$ to $\approx 0.1\text{\AA}$ at $z = 0$. The redshift dependence of W_r^* in our LCDM model can be crudely characterized as

$$W_r^* \sim 0.1 \times (1 + z)^{0.1}. \quad (6)$$

The other models produce a roughly similar dependence, so this result is fairly insensitive to the cosmology. However, it does depend on the high spectral resolution adopted for our artificial spectra.

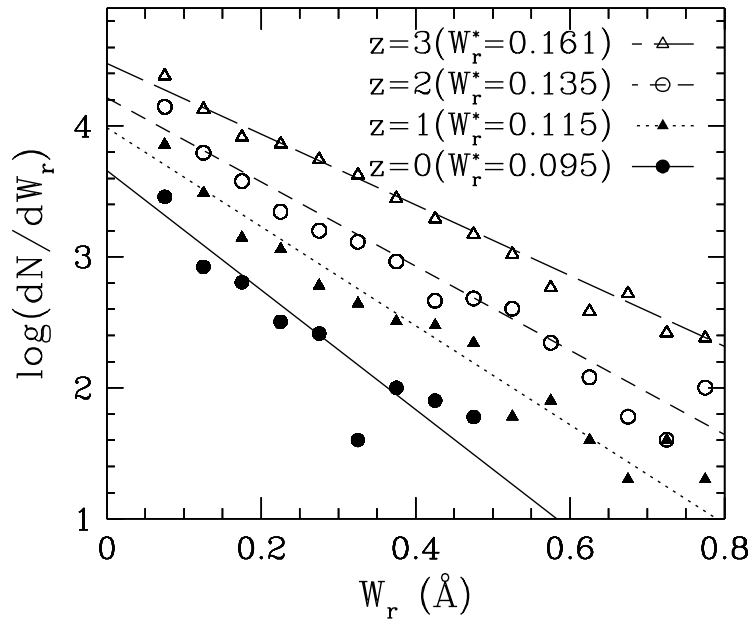


Fig. 8.— Equivalent width distributions at $z = 3, 2, 1, 0$ in the LCDM model. The best-fit value of W_r^* (eq. [5]) at each redshift is shown in the legend. The redshift dependence can be roughly parameterized as indicated in equation (6).

To investigate the spectral resolution issue we generated artificial spectra at $z = 0$ with a resolution of 230 km s^{-1} (comparable to FOS). These lower resolution spectra are well fit by an exponential distribution with a larger value of $W_r^* \approx 0.26$ (except with a significant turnover for $W_r \lesssim 0.1 \text{ \AA}$ caused by incompleteness). $W_r^* \approx 0.26$ is in reasonable agreement with W98, who find $W_r^* = 0.283 \pm 0.012$. Thus, the discrepancy between equation (6) and the (larger) values of W_r^* deduced from the observations apparently reflects the influence of line blending rather than a fundamental failing of the cosmological models. A direct test of the simulations on the basis of the equivalent width distribution will require a closer match of resolution and noise properties between artificial and observed spectra, which we defer to future work.

The steepening of dN/dW_r implies that strong Ly α absorbers evolve more rapidly than weak ones. This trend is consistent with W98, who find that γ is larger for higher equivalent width absorbers. Using equation (6), we predict the values of γ for the redshift range $z = 1.5$ to $z = 0$ in different equivalent width regimes¹, analogous to Figure 7 of W98. The results are shown in Figure 9. While the trend from artificial spectra (open circles) is qualitatively similar to observations (filled squares with error bars), the data appear to show a more dramatic decrease in γ for low- W_r lines. Note that the simulation results are derived directly from equation (6), so the effects of spectral resolution (i.e., blending) and lack of sensitivity to small equivalent widths (i.e., incompleteness) are probably significant. Hence it is unclear whether this represents a failing of the model or systematic differences between the artificial spectra and the FOS data. In any case, the statistical significance of the discrepancy is barely 1σ .

There is further observational evidence that the equivalent width distribution steepens at lower redshift. The column density slope found for the $\langle z \rangle = 1.9$ spectrum of Q1331+170 (Kulkarni et al. 1996) is steeper than that typically found at $z \sim 3$ (e.g. KHCS). At even larger W_r , Lyman limit systems (LLS) are seen to evolve more rapidly than Ly α forest absorbers at low redshifts ($\gamma_{\text{LLS}} = 1.5 \pm 0.39$; Stengler-Larrea et al. 1995). It is less straightforward to count LLS in our simulations because the effects of neutral hydrogen self-shielding and the contribution from low mass objects must be taken into account (e.g., Gardner et al. 1997a); nevertheless, we are planning a careful examination of their redshift evolution in the future.

The J_ν evolution scenario, which approximately describes the evolution of dN/dz , predicts the same value of γ for all equivalent width limits. The trend of steeper evolution for stronger Ly α absorbers probably reflects the physics of gravitational structure formation. Regions of higher density expand more slowly than regions of lower density owing to their stronger self-gravity. As we shall show in §4.1, lower density gas gives rise to weaker Ly α absorbers. Thus the fractional cross-section of weaker Ly α absorption increases with time relative to that of stronger Ly α absorption, giving rise to preferentially more weak absorbers at low- z . While structure formation plays a subordinate role to the ionizing background in the evolution of dN/dz , it is central to the

¹We cannot determine this relationship directly from our spectra up to the highest values of W_r explored by W98 because we have very poor statistics for lines with large W_r .

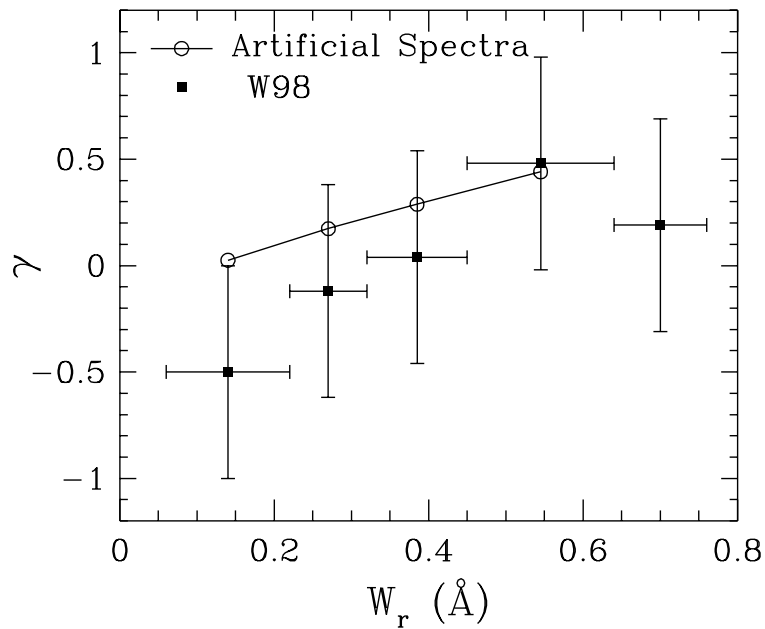


Fig. 9.— Equivalent width vs. γ (defined in eq. [1]), as predicted from equation (6). The observations of W98 are shown as solid squares with error bars. The value of γ is larger for strong absorbers, indicating that they evolve more rapidly than weak absorbers. More sensitive observations at low- z should reveal a large population of weak lines.

evolution of W_r^* .

Equation (6) implies that at low redshift, the Ly α forest should be even more dominated by weaker absorbers than it is at high redshifts. Using GHRS data, TLS estimate $dN/dz = 102 \pm 16$ for lines with $W_r > 0.05\text{\AA}$ and $0 < z < 0.28$, about three times higher than the value that W98 find for $W_r > 0.24\text{\AA}$. Equation (6) predicts a ratio of $e^{(0.24-0.05)/0.1} = 6.7$, which suggests that the equivalent width distribution predicted by the simulations is excessively steep. Assessment of this possible discrepancy will require more detailed consideration of spectral resolution effects. Higher resolution data from STIS should eventually yield more accurate measurements of the population of weak lines.

4. Physical Evolution of the Absorbing Gas

4.1. Column Density vs. Overdensity

One of the most illuminating results to emerge from hydrodynamic simulations of the high-redshift Ly α forest is the existence of a tight correlation between the HI column density of an absorption feature and the average or peak gas density of the structure that produces it (see, e.g., Zhang et al. 1995; Miralda-Escudé et al. 1996; Hellsten et al. 1998). In principle, the column density of an absorber can be affected by its density and temperature (which together with Γ_{HI} determine the neutral fraction and neutral gas density) and by its line-of-sight spatial extent (since the product of spatial extent and neutral gas density yields the neutral column density). However, the competition between photoionization heating and adiabatic cooling leads to a tight correlation between temperature and density for the unshocked gas that produces most of the high- z Ly α forest absorption (Hui & Gnedin 1997), thus linking two of the three parameters. Variations in the line-of-sight spatial extent remain a source of scatter, but they are small compared to the range of neutral gas densities.

Figure 10 plots the overdensity $\rho_H/\bar{\rho}_H$ against neutral column density N_{HI} for absorbers at $z = 3, 2, 1$, and 0 in the LCDM model. For purposes of this figure, we identify absorbers directly from the simulation output (without noise or continuum fitting) using the method of Hellsten et al. (1998): lines are identified as peaks in the optical depth, and the column density is summed outwards from the peak until a local maximum is reached.

There is a clear correlation between overdensity and neutral column density at each redshift shown in Figure 10. The scatter increases at lower redshifts mainly because (as we will show below) shock heated gas makes a larger contribution to the Ly α forest. Shock heating lowers the neutral fraction at a fixed density, and the outliers in Figure 10 almost all lie at column densities that are lower than the mean trend.

The solid lines in Figure 10 show a power law fitted to the data points at each redshift. The dotted lines show the fits from the other redshifts, for comparison. The exponent remains roughly

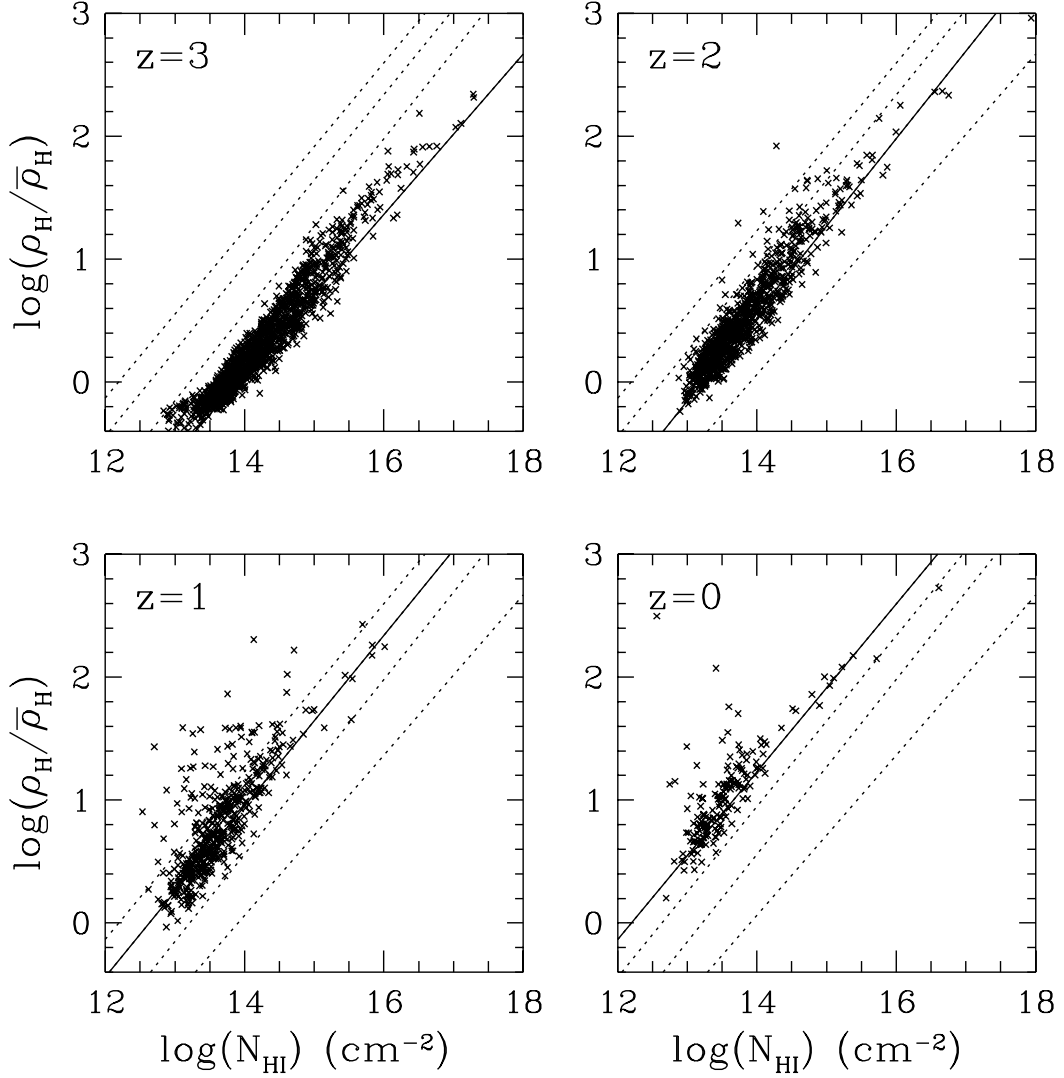


Fig. 10.— The relation between gas overdensity and column density for the LCDM model, at $z = 3, 2, 1$, and 0 . The physics of the photoionized IGM leads to a power law relation that has roughly constant index, but the overdensity associated with a given column density increases with decreasing z . The solid line in each panel shows the best-fit power law at each redshift, while the dotted lines show the fits from other redshifts. Collapsed objects such as galaxies form at overdensities $\gtrsim 100$, implying that low- z absorbers will be more correlated with galaxies at a given

constant with $\rho_H/\bar{\rho}_H \propto N_{\text{HI}}^{0.7}$, but the overdensity associated with a typical absorber of given N_{HI} increases significantly at low redshifts. The physics behind this change is the same physics that underlies our discussion of dN/dz evolution in §3.4: the physical density associated with a given overdensity falls as the universe expands, and the resulting decline in recombination rate is only partly compensated by the decline in photoionization rate. The mean trends shown in Figure 10 can be approximately summarized by the formula

$$\delta_H \equiv \frac{\rho}{\bar{\rho}_H} \sim 20 \left[\frac{N_{\text{HI}}}{10^{14} \text{cm}^{-2}} \right]^{0.7} 10^{-0.4z}. \quad (7)$$

The redshift dependence in equation (7) depends on the UV background history — in this case taken from HM — but it is similar in all four of our cosmological models. The overall scaling factor depends on the mean flux decrement normalization, which in this case is based on Rauch et al.’s (1997b) determination at $z = 3$. Bryan et al. (1998), for example, find a significantly higher overdensity at specified column density at $z = 3$ than equation (7) implies because their mean flux decrement is substantially lower, $\bar{D} = 0.214$ instead of $\bar{D} = 0.32$ (the Rauch et al. 1997b value, which we adopt here) or the earlier estimate $\bar{D} = 0.36$ by Press, Rybicki, & Schneider (1993).

Figure 10, and its summary in equation (7), is the key to understanding the physical relation between the low- z Ly α forest and the high- z Ly α forest. The dynamical state of an absorber — expanding or collapsing, unshocked or shocked — depends mainly on its overdensity. A specified column density range picks out absorbers of progressively higher overdensity and progressively more advanced dynamical states as the universe expands. A $z = 0$ Ly α absorber is physically analogous *not* to a $z = 3$ Ly α absorber of the same column density but to a $z = 3$ absorber with column density $10^{0.4 \times 3/0.7} \approx 50$ times higher. In a less quantitative form, this transformation could be seen already in Figures 2 and 6, where the different redshift panels seem to show similar underlying structure with a steadily shifting color map, corresponding to the changing relation between overdensity and column density.²

To put these results in a specific context, it is useful to recall that the $W_r \sim 0.24\text{\AA}$ equivalent width limit typical of the Key Project FOS spectra corresponds to $N_{\text{HI}} \sim 10^{14} \text{cm}^{-2}$ for a b -parameter of 30 km s^{-1} . The Key Project spectra identify many lines weaker than 0.24\AA as well, but the largest uniform detection limit sample is for this equivalent width limit. At $z = 3$, this column density would be produced by gas near the cosmic mean density, but at $z = 0$ it requires gas of overdensity $\delta_H \approx 20$, which corresponds to $N_{\text{HI}} \sim 10^{15.5} - 10^{16} \text{cm}^{-2}$ at $z = 3$. Higher resolution spectra measured with GHRS can detect lines down to $N_{\text{HI}} \sim 10^{13} \text{cm}^{-2}$, corresponding to an overdensity of a few at $z = 0$. Future observations using STIS, and eventually COS, should be able to quantify the population of Ly α absorbers tracing these low-density regions quite accurately.

²For a similar reason, the relation between the $z = 1$ and $z = 3$ panels of Figure 2 is reminiscent of the relation between the HI and HeII opacity maps at $z = 2.33$ shown in figure 2 of Croft et al. (1997b).

4.2. Evolution of Gas Phases

Figure 11 plots the positions of SPH particles (a 1/50th subset) from the LCDM simulation in the overdensity–temperature plane, at $z = 3, 2, 1$, and 0. At each redshift, the gas is distributed among three broadly defined phases (KWH):

1. “Diffuse”– a cool, low density phase associated with gas whose temperature is determined by the competition between photoionization heating and adiabatic cooling;
2. “Shocked”– a hot, intermediate density phase consisting of shock-heated gas in filaments and in galaxy, group, and cluster halos; and
3. “Condensed”– a cold, dense phase associated with gas in galaxies.

Gravitational collapse moves gas from the diffuse phase to the shocked phase, and radiative cooling moves gas from the shocked phase to the condensed phase.

The lines in Figure 11 demarcate density and temperature regions that roughly correspond to the three phases listed above. The lower left region corresponds to the diffuse phase, the upper region corresponds to the shocked phase, and the lower right region corresponds to the condensed phase. Gas in the condensed phase is defined to have $T < 30,000\text{K}$ and an overdensity greater than 100.

Figure 12 shows the evolution of the baryonic mass fraction in each phase, in our four cosmological models. Here we include the stellar mass component as part of the condensed phase. At all redshifts, a large fraction of the baryons in the universe resides in the diffuse phase. By $z = 0$ the fractions of baryons in the condensed and shocked phases are comparable. Note that the rate of evolution of the gas is fairly model dependent, with the $\Omega = 1$ models showing more late, rapid evolution and the low- Ω models tending to form galaxies and filamentary structure earlier.

To see how the character of the Ly α forest absorbers evolves, we examine the fraction of absorbers arising from each gas phase as a function of redshift. We first assign every absorber identified in our 400 random LOS a density and temperature. This is done by determining the velocity at which the neutral hydrogen density is maximum within $2b$ of the absorber’s central velocity (where b is the b -parameter) and assigning the absorber’s density and temperature to be the values at this maximum. Using this density and temperature and the demarcation in Figure 11, we determine the phase of gas that is predominantly responsible for giving rise to the absorber.

The left panels of Figure 13 show the fraction of weak ($W_r \leq 0.24\text{\AA}$) and strong ($W_r > 0.24\text{\AA}$) absorbers in each of the three phases as a function of redshift. The weak absorber population is dominated by diffuse gas at all redshifts, although the contribution of shocked gas grows with time. The strong absorber population undergoes a marked transition from predominantly diffuse gas at $z > 2$ to predominantly shocked gas at $z \leq 2$. This transition is much sharper than the

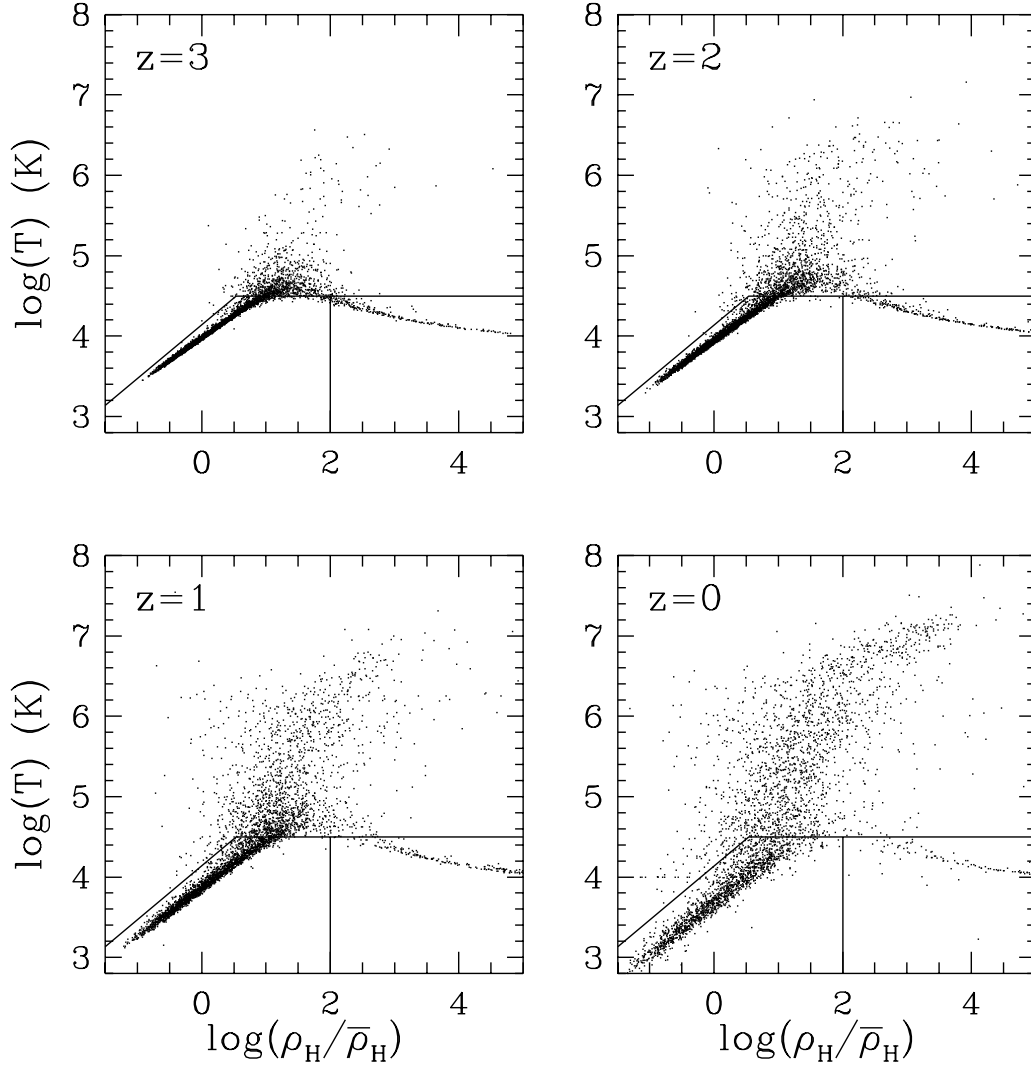


Fig. 11.— Temperature vs. overdensity at $z = 3, 2, 1,$ and 0 , in the LCDM model. The plot shows a randomly selected, $1/50^{\text{th}}$ subset of the gas particles. The gas resides in three general phases: cool, photoionized, diffuse IGM (tail to lower left), shocked IGM, and condensed (tail to lower right). Lines indicate approximate demarcations between these phases.

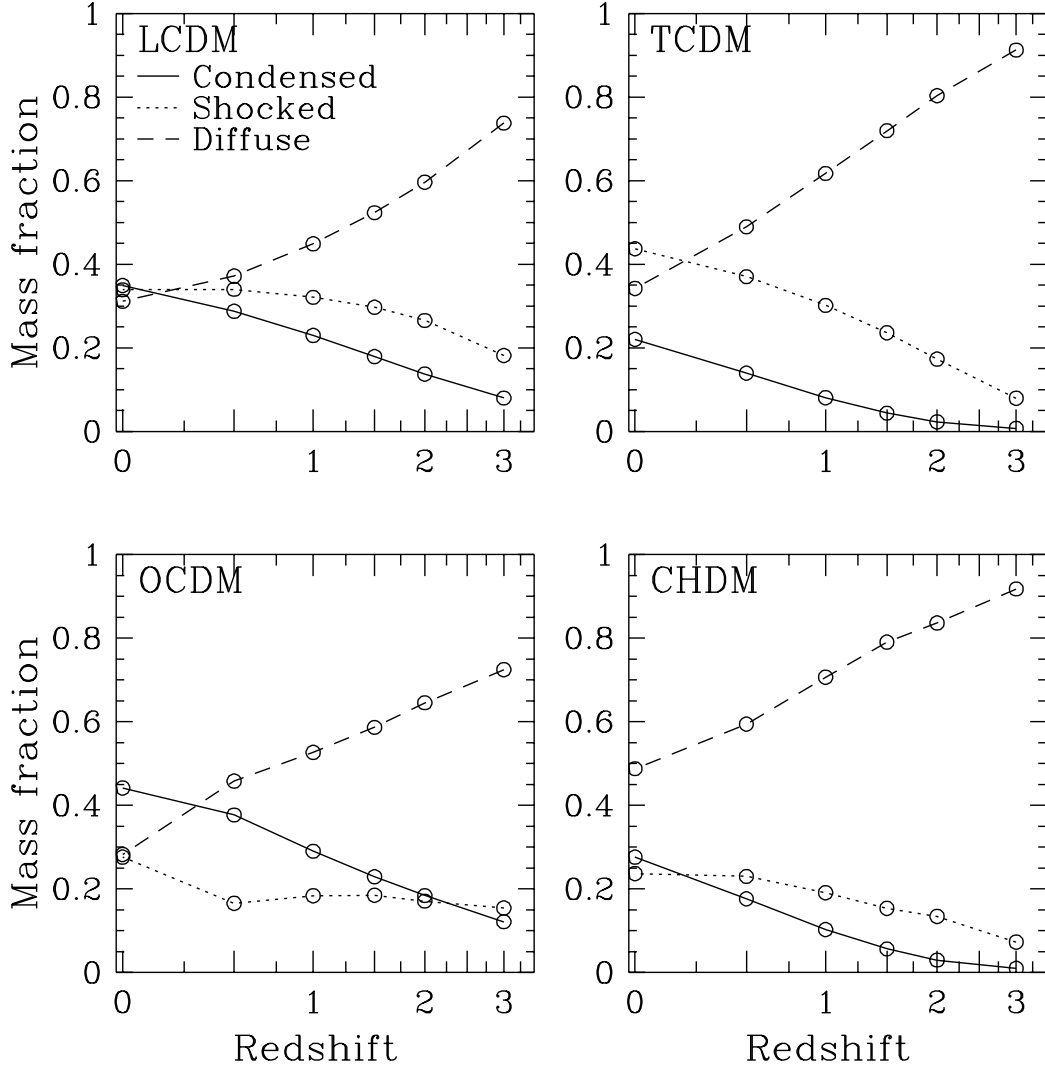


Fig. 12.— Evolution of the baryonic mass fraction in the three phases indicated in Fig. 11. Above $z \sim 1$, diffuse IGM gas dominates in all the models. By $z = 0$, mass fractions in three phases are comparable (with some model dependence). At all redshifts, the diffuse component contains a significant fraction of the baryonic mass in the universe.

change in the global gas fractions (Figure 12), and it occurs for the reasons already discussed in §4.1: the 0.24\AA equivalent width threshold picks out absorbers of higher overdensity at lower redshift, and gas with $\delta_H < 10$ is typically unshocked and gas with $\delta_H > 10$ is typically shocked (Figure 11). We demonstrate this point in the right hand panels of Figure 13, which show the evolution of the phase distribution for absorbers with $\delta_H < 10$ (top) and $\delta_H > 10$ (bottom). With this division, there is only weak evolution in the fraction of absorbers in different phases. In other words, Ly α absorbers do not change character from high to low redshift if one selects on overdensity (which is not directly observable), but lines of specified equivalent width or column density trace different physical structures at different redshifts.

Although we use the LCDM model for Figure 13, we find similar trends in all of our models. Only a rather small fraction of the strong absorbers arise from condensed gas, even at $z = 0$, although if we raised the equivalent width threshold the fraction of condensed absorbers would increase. Our conclusion that shocked gas begins to dominate the absorber population at $z \lesssim 2$ for $W_r > 0.24\text{\AA}$ is similar to that of Riediger et al. (1998, figure 6). However, our interpretation of this result is rather different. The cause of the transition is not that unshocked absorbers evolve faster than shocked absorbers but that the equivalent width threshold (or column density threshold in Riediger et al.’s analysis) selects a different subset of the absorber population at different redshifts.

5. Low-Redshift Ly α Absorbers and Galaxies

5.1. Observations

Do Ly α absorbers at low redshift arise predominantly in galaxy halos? This question has been the focus of a number of observational studies. LBTW imaged 46 galaxies ($0.07 \lesssim z \lesssim 0.55$) in six fields around Key Project spectroscopic target quasars and argued that galaxies generally produce associated Ly α absorption out to projected separations $r_p \sim 160h^{-1}$ kpc, and that at least one-third of all Ly α absorbers are physically associated with galaxies (i.e., arise from gas bound to galaxy potentials). CLWB extended this work and found a strong correlation of increasing equivalent width with decreasing impact parameter to the nearest galaxy³, strengthening the case for an association between galaxies and Ly α absorbers out to $z \sim 0.8$. Recently TLS showed that this correlation extends much further than found by CLWB, to impact parameters of $\sim 500h^{-1}$ kpc. However, numerous observations reveal Ly α absorption occurring with no nearby galaxy (e.g., Morris et al. 1993; van Gorkom et al. 1996; Bowen, Pettini, & Boyle 1998), and it has been suggested that only the stronger Ly α absorbers are associated with galaxies, whereas weaker ones routinely occur even in voids (Stocke et al. 1995; SSP; Grogin & Geller 1998). A plausible

³This trend is frequently described in the literature as an anti-correlation, but we prefer to describe it as a correlation of increasing W_r with decreasing r_p to emphasize the expected signature of increased gas density close to galaxies.

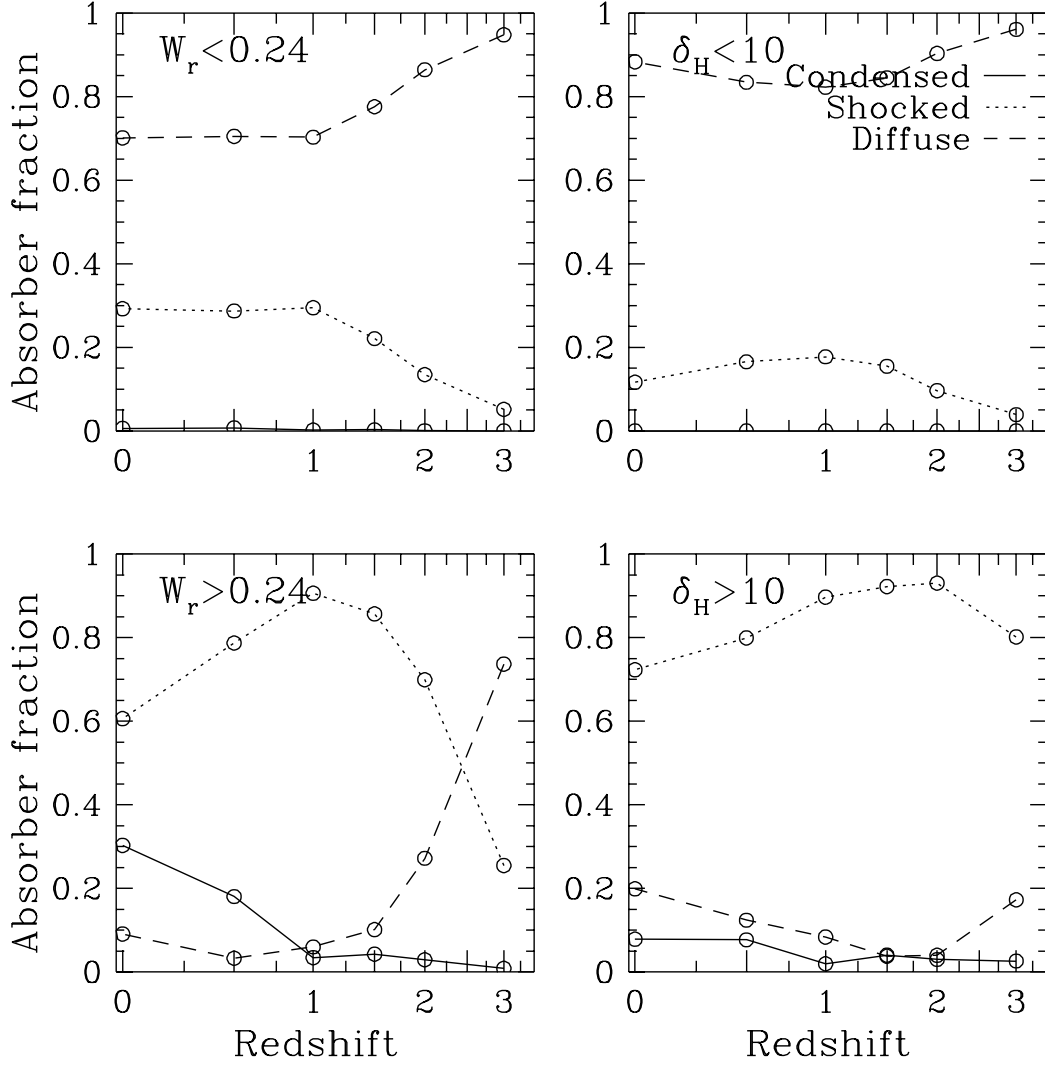


Fig. 13.— Evolution of the fraction of absorbers associated with gas phases indicated in Fig. 11, for the LCDM model. *Left panels:* Weak absorbers with $W_r < 0.24 \text{ \AA}$ arise predominantly in diffuse gas at all redshifts, while stronger absorbers are progressively more dominated by shocked gas at lower redshifts. *Right panels:* Viewed by physical density rather than W_r , absorbers show much less evolution, with low density absorbers ($\delta_H < 10$) dominated by diffuse gas at all z and high density absorbers ($\delta_H > 10$) dominated by shocked gas at all z . Absorption from condensed gas in galaxies makes a small contribution at all redshifts.

population of low surface brightness galaxies has a covering fraction that can account for Ly α absorber counts (CLWB; Linder 1998), but deep observations have failed to detect such galaxies around absorbers (Rauch, Weymann, & Morris 1996). Conversely, various observations suggest that Ly α absorbers at low redshift typically arise in filamentary and sheet-like networks tracing large scale structure (Le Brun et al. 1996; Dinshaw et al. 1997; Le Brun & Bergeron 1998), similar to the structures that simulations predict at high redshift.

While some of these findings at face value seem contradictory, the variety of the observational procedures, selection effects, and sensitivity make it difficult to directly compare results. In this section, we examine the relationship between Ly α absorbers and galaxies in our simulations, with the goal of providing interpretations for these observations within the context of hierarchical structure formation models.

5.2. Identifying Galaxies

To identify clumps of gas and stars in our simulations that are likely to correspond to galaxies, we use the galaxy identification algorithm SKID (KWH; <http://www-hpcc.astro.washington.edu/tools/SKID>), which is a modified version of DENMAX (Gelb & Bertschinger 1994). SKID identifies galaxies as gravitationally bound groups of 16 or more cold gas ($T < 30,000$ K and $\rho/\bar{\rho} > 170$) and star particles that are associated with a common density maximum (corresponding to a minimum baryon mass $M_b \sim 1.7 \times 10^9 M_\odot$ in the LCDM model). SKID computes a number of physical properties of these groups, including mass, center-of-mass position and velocity, maximum circular velocity, half-mass radius, and maximum radial extent.

We also identify the halos of dark and baryonic matter associated with the cold, dense gas in galaxies. We again use SKID for this purpose, but we now apply it to all the particles in our simulations, including dark matter, stars, and hot and cold gas. The maximum radial extent is the distance from the center of mass to the outermost bound particle, and it corresponds to the bound extent of the halo.

Figure 14 shows distributions of the mass and bound extents of halos with different numbers of galaxy subcomponents, for the LCDM model at $z = 1$ and $z = 0$. Some halos have no baryonic subcomponent; this is purely a resolution effect. A small number of halos (mostly larger, more massive ones) have multiple galaxies. Very rarely, a galaxy is found by SKID that has no accompanying SKID-identified halo. For the majority of cases, however, there is a one-to-one correspondence between halos and galaxies. Figure 15 (which will be discussed in more detail in the next section) shows the galaxies as crosses and the (independently identified) halos as circles whose radius corresponds to the halo’s bound extent; note the good agreement between the center-of-mass positions of galaxies and halos.

Figure 14 indicates that the smallest resolved galaxies in our LCDM simulation have masses

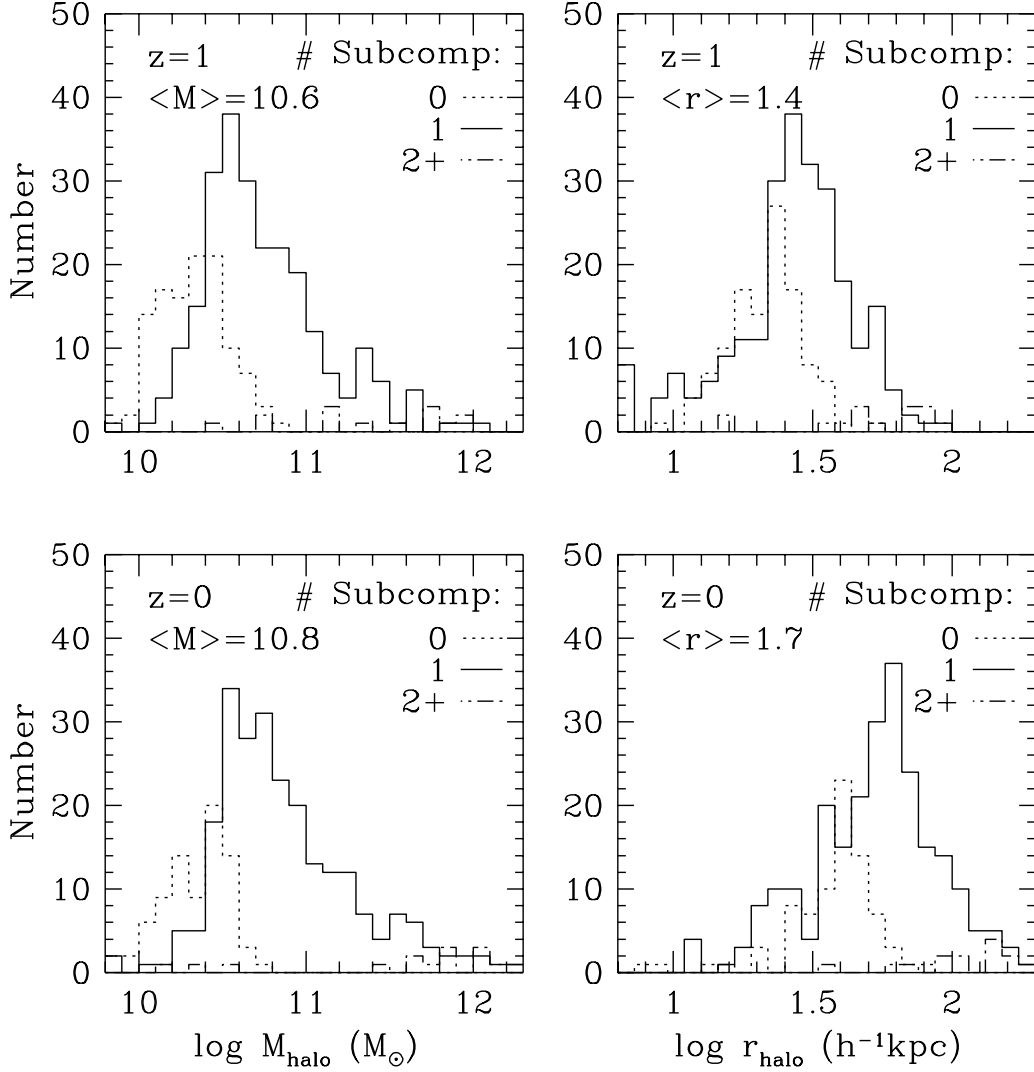


Fig. 14.— Histograms of dark halo masses and outer radii (bound extents), for the LCDM model at $z = 1$ and $z = 0$. Left panels show the dark halo mass, for halos with no identified baryonic galaxy (dotted histogram), one galaxy (solid), and more than one galaxy (dashed). The typical halo mass (in $\log M_{\odot}$) is shown in the upper left. Right panels are corresponding plots for outer halo radii (typical value shown in $h^{-1} \text{kpc}$).

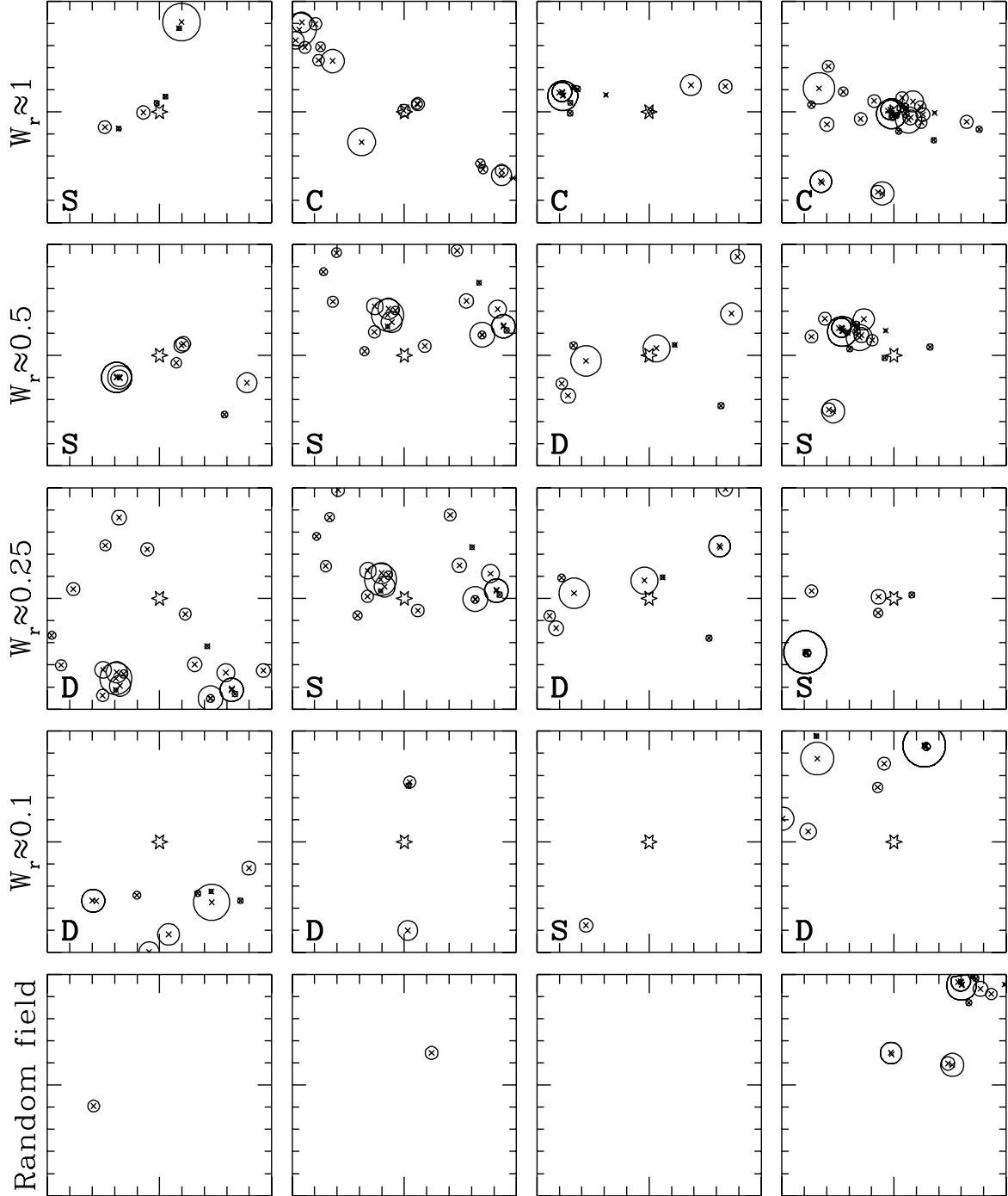


Fig. 15.— Galaxy fields ($2 \text{ Mpc} \times 2 \text{ Mpc}$) from the LCDM model at $z = 0$ surrounding a sample of four random LOS from each equivalent width range listed along the left. The central star represents the LOS position. Galaxies within 200 km s^{-1} of the absorber redshift are shown as crosses, with surrounding circles indicating the maximum extent of the dark halo. The absorber gas phase is indicated in the lower left: D=Diffuse, S=Shocked, C=Condensed. The bottom row shows a random sample of fields for comparison.

$\sim 2 \times 10^{10} M_{\odot}$ of total (dark+baryonic) mass. These galaxies are significantly smaller and more numerous than L^* galaxies. The halo radii are typically quite small, rarely exceeding $100h^{-1}$ kpc even at $z = 0$.

5.3. A Sample of Galaxy Fields Around Absorbers

Figure 15 shows a mosaic of $2 \text{ Mpc} \times 2 \text{ Mpc}$ galaxy fields, each centered on an absorber taken from our 400 random LOS in the LCDM model at $z = 0$. The central star marks the position of the absorber (and thus of the artificial quasar in the background). Crosses show galaxies identified by SKID that are within 200 km s^{-1} of the absorber redshift, and the circles show the dark halos associated with these galaxies. The circle radius corresponds to the maximum bound extent of the halo. Each row shows four absorbers that have equivalent widths close to that listed on the left of the plot. The absorbers in the top row are the four strongest absorbers from the random LOS. For comparison, the bottom row shows four fields selected at random without regard to the presence of an absorber; they have no central star since there is no absorber there. Finally, the letter in the lower left indicates the absorber’s gas phase: D=Diffuse, S=Shocked, C=Condensed. These panels may be compared with, for instance, Figures 3–8 of LBTW showing imaged quasar fields.

The strongest absorbers most often arise from condensed gas in galaxies, and, less frequently, from shocked gas close to galaxies. At somewhat lower W_r , most of the absorbers are associated with shocked gas in extended large scale structure around galaxies but do not lie within the bound extent of a dark halo. Absorbers with $W_r \lesssim 0.3\text{\AA}$ are typically associated with diffuse gas and tend to lie further away from galaxy concentrations. Still, even at $W_r \sim 0.1\text{\AA}$, absorbers reside in regions where there are typically more galaxies than would be seen randomly (cf., bottom panels). This figure suggests that while most Ly α absorbers do not arise directly from gas in galaxies, they do tend to cluster around galaxies. This figure and discussion are for the LCDM model at $z = 0$, but the trends are similar in all cosmologies.

5.4. Galaxy Slices With Lines of Sight

Figure 16 shows four 2 Mpc –thick slices through the LCDM simulation volume at $z = 0$, with 10 LOS in each slice (shown as the dotted lines). The slices are taken along the simulation’s z -axis (into the page), the y -axis is vertical, and the x -axis positions of galaxies have been shifted into redshift space using the center-of-mass velocity of the galaxy. The LOS are taken from the random sample of 400, and are selected as those 10 that have z positions closest to the center of the slice. As in Figure 15, galaxies are shown as circles with the radius corresponding to the dark halo’s maximum bound extent. The absorbers identified by AutoVP along each random LOS are shown as diamonds, with the linear size of the diamond proportional to $\log(W_r)$. The size representing a $W_r = 0.24\text{\AA}$ absorber is shown in the upper left panel. Note that the simulation volume, and thus

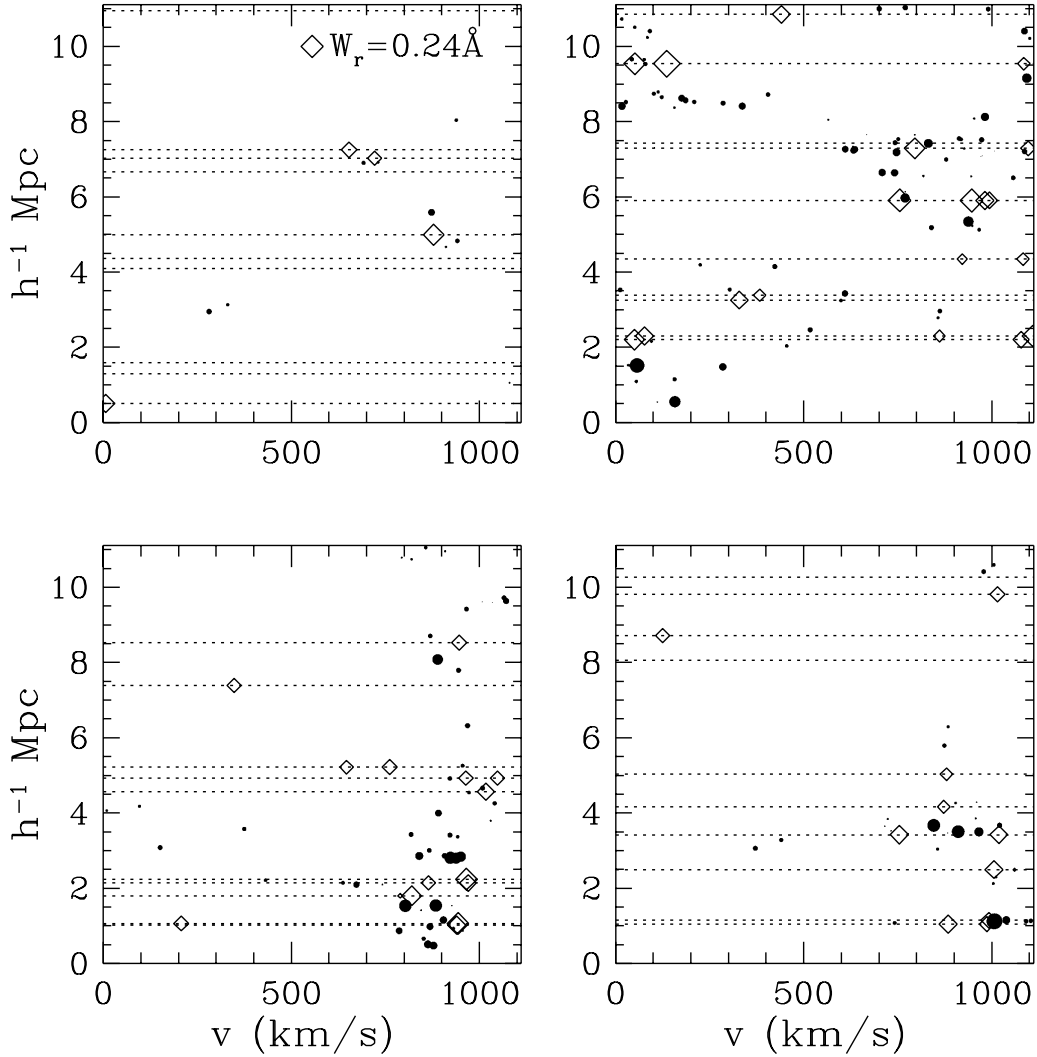


Fig. 16.— Four slices (2 Mpc thick each) through the LCDM simulation volume at $z = 0$, with the ten random LOS nearest to the middle of the slice shown as dotted lines. Absorbers identified with AutoVP are shown as diamonds, with linear size proportional to $\log(W_r)$ (see upper left panel for scale). Galaxies are shown as filled circles, with radius corresponding to maximum halo extent.

each panel, is periodic in every direction. These panels are comparable to, for example, the pie diagrams (figure 3) in SSP.

From Figure 16, we see that Ly α absorption occurs in a variety of environments, with significant absorption sometimes occurring with no nearby galaxy. The lower left panel shows a number of absorbers associated with the filamentary structure down the right side of the volume. Nearby LOS sometimes show absorbers along both LOS, and sometimes only along one. This is a real effect, not an artifact of the line identification or fitting procedure.

Like Figure 15, Figure 16 suggests that absorbers do tend to correlate with large scale structure but that very few absorbers arise directly from gas in galaxy halos. It also shows that some absorbers arise in void-like regions in our simulations.

5.5. The Absorber-Galaxy Cross-Correlation Function

To quantify the visual impressions of Figures 15 and 16, that low-redshift Ly α absorbers tend to arise from gas near but not gravitationally bound to galaxies, we measure the cross-correlation function of galaxies and Ly α absorbers. We define the absorber-galaxy cross-correlation function by

$$\xi(r_p, v) = \frac{N_{\text{pairs}}}{N_{\text{rand}}} - 1, \quad (8)$$

where N_{pairs} is the number of absorber-galaxy pairs in our simulations having projected separations between r_p and $r_p + \Delta r_p$ and line-of-sight velocity separations between v and $v + \Delta v$, and N_{rand} is the number of pairs expected for randomly distributed absorbers. We find N_{pairs} by taking each absorber in our 400 random LOS, finding r_p and the velocity difference to each galaxy, and binning the pairs in $100h^{-1}$ kpc and 100 km s^{-1} intervals. N_{rand} is determined by choosing a random position within the simulation volume for each absorber and performing the same procedure.

Figure 17 shows $\xi(r_p, v)$ as a contour plot in r_p and v , for absorbers with $W_r < 0.24\text{\AA}$ (upper panels) and $W_r > 0.24\text{\AA}$ (lower panels), at $z = 1$ (left panels) and $z = 0$ (right panels), for the LCDM model. Contour levels are $\xi = 1, 2, 3, 4, 5, 6$, where odd levels are dotted lines. For instance, the outermost contour ($\xi = 1$) represents the locus of (r_p, v) points where the probability of finding a galaxy around an absorber is enhanced by a factor of two. Note that the y -axis shows a v range corresponding to half the simulation box length, while r_p only goes out to $1.5h^{-1}$ Mpc (comoving), or 14% of the box length.

The value of $\xi(r_p, v)$ increases towards smaller velocity separations and smaller impact parameters, as expected. There is a decline in the number of absorber-galaxy pairs at small impact parameter ($r_p \lesssim 100h^{-1}$ kpc), and to a lesser extent at small velocity separation ($v \lesssim 100 \text{ km s}^{-1}$), perhaps because the strong, saturated absorbers near galaxies (discussed in §5.6 below) tend to subsume other nearby absorbers. In most cases, $\xi > 1$ out to projected separations of $r_p \sim 1h^{-1}$ Mpc or more. At small r_p , the correlation function exceeds unity out to velocity

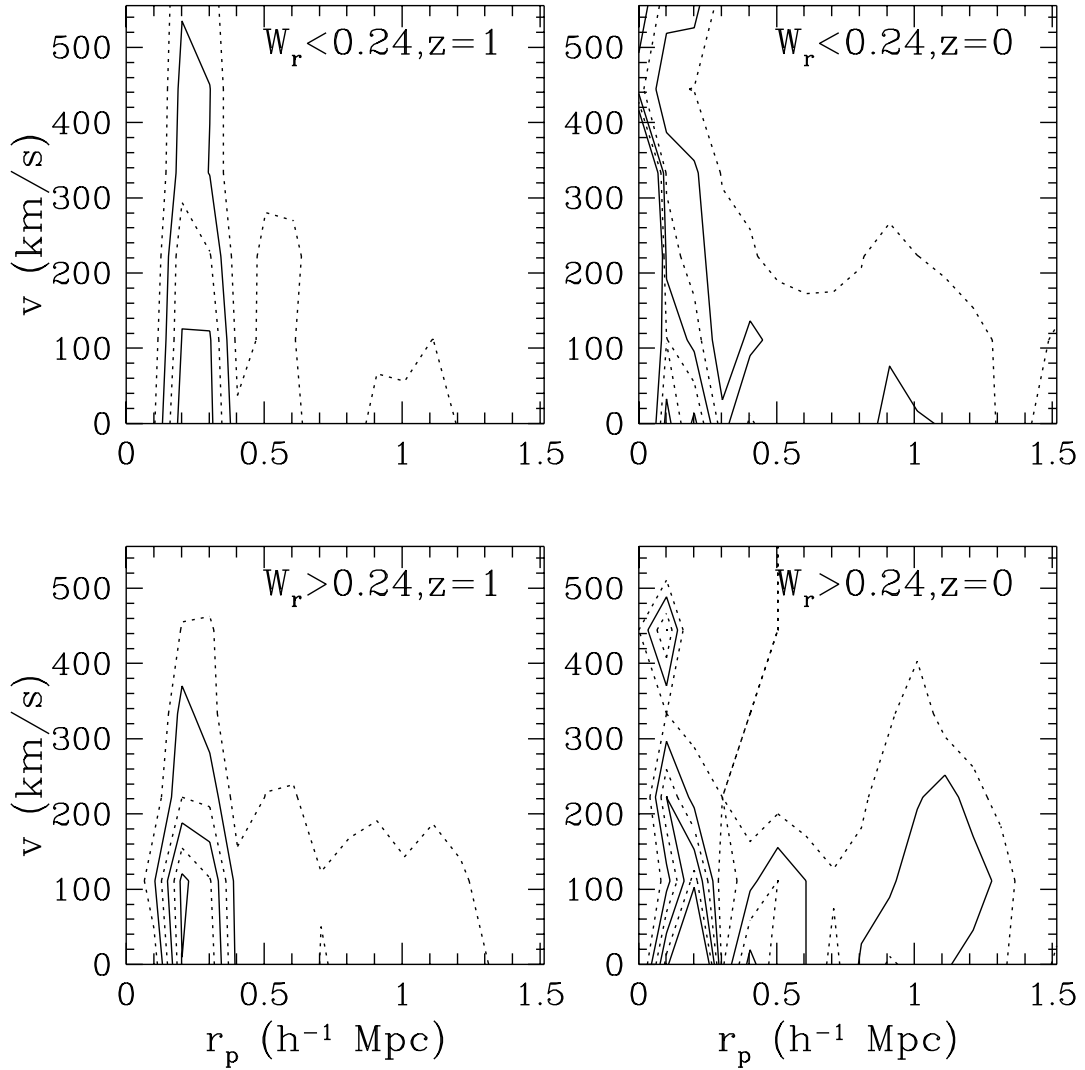


Fig. 17.— Absorber-galaxy cross-correlation function $\xi(r_p, v)$, as defined in §5.5, for the LCDM model: Top and bottom panels show absorbers with $W_r < 0.24\text{\AA}$ and $W_r > 0.24\text{\AA}$, respectively. Left and right panels are for $z = 1$ and $z = 0$, respectively. Contours show values of $\xi(r_p, v) = 1, 2, 3, \dots$, with dotted contours representing odd values and solid contours even values.

separations of at least 400 km s^{-1} . The correlation function is highly elongated along the velocity axis because of the peculiar velocity of gas surrounding galaxies. The noise in these plots is dominated by the finite number of independent structures in our simulation volume, not by the shot noise in the number of absorber-galaxy pairs.

The correlation function of strong absorbers (lower panels) is stronger than that of weak absorbers (upper panels). For example, at $z = 1$ the peak value of $\xi(r_p, v)$ is 6 for strong absorbers but 4 for weak absorbers. However, the difference is not dramatic, at least for the W_r division adopted here, and it appears that the clustering of the large scale gas distribution with galaxies gives rise to some spatial correlation for all absorbers, regardless of their strength. In short, Ly α absorbers are correlated significantly with galaxies out to separations of at least $400h^{-1} \text{ kpc}$, well beyond the physical extents of the galaxies themselves.

The cross-correlation function defined by equation (8) is one of the cleanest statistics for quantifying the relation between the absorber and galaxy populations. It does not require a distinction between “associated” and “unassociated” pairs, and the normalization to a random population makes it relatively insensitive to the details of sample selection (e.g., the magnitude limit of the galaxy survey). With enough data, the cross-correlation can be determined as a function of both absorber equivalent width and galaxy luminosity. Morris et al. (1993) studied a one-dimensional version of the cross-correlation function, combining r_p and v separations to estimate an absorber-galaxy distance. Lanzetta et al. (1998) have presented preliminary observational results for $\xi(r_p, v)$; our $\xi(r_p, v)$ predictions appear roughly consistent with these data, but perhaps somewhat weaker at small separations.

The distribution of galaxy densities around absorbers (Grogin & Geller 1998) is a statistic with many of the same virtues as $\xi(r_p, v)$. It responds to high-order correlations as well as two-point correlations, and it is especially well suited to characterizing the relations between the absorber and galaxy populations on large scales. Unfortunately, our current simulations are too small to apply this statistic, at least with the $5h^{-1} \text{ Mpc}$ smoothing scale adopted by Grogin & Geller (1998). The line-of-sight autocorrelation function of absorbers is much more sensitive to line-blending effects than the absorber-galaxy cross-correlation function because blending eliminates precisely the pairs that one is attempting to count (see, e.g., Ulmer [1996] for a measurement using the Key Project data set and for a discussion of blending effects). We do not present autocorrelation results here because even a qualitative comparison to observations requires detailed modeling of the data properties and line identification procedure. We suspect that statistics that treat the absorption spectrum as a continuous one-dimensional field (e.g., Croft et al. 1997a; Rauch et al. 1997b; Croft et al. 1998; Miralda-Escudé et al. 1998) will ultimately prove more powerful than line correlations for characterizing large scale clustering in the Ly α forest.

5.6. Impact Parameter vs. Equivalent Width

The correlation of increasing equivalent width with decreasing impact parameter is a key piece of evidence cited by CLWB in support of the hypothesis that low-redshift Ly α absorbers arise in extended gaseous envelopes of galaxies. In order to approximately mimic the procedure of CLWB, we find the galaxy whose outer radius (defined by the star or cold gas particle furthest from the center of mass) has the smallest projected distance to the LOS, for each of the 400 random LOS through the simulation. We fit all HI features within 200 km s $^{-1}$ (or, if greater, the maximum rotational velocity) of the redshift-space velocity of the galaxy, and sum the equivalent widths of all identified lines⁴. We identify this summed complex as a single absorber, since current (FOS) observations are typically unable to resolve lines within ~ 200 km s $^{-1}$. For each absorber, we find the peak neutral density within 200 km s $^{-1}$ and use the gas density and temperature at this peak to define the absorber’s gas phase (cf. §4.2). To better sample the regions near galaxies, we generate 400 “selected” LOS chosen to have $10 < r_p < 100h^{-1}$ kpc from a galaxy, and we apply the same procedure. Since the probability of a random LOS passing so close to a galaxy is fairly small, most LOS having $r_p < 100h^{-1}$ kpc are selected LOS.

The top panels of Figure 18 show a scatter plot of W_r vs. r_p for LOS drawn from the LCDM model at $z = 1$ and $z = 0$. Filled circles indicate absorbers arising from condensed gas, open triangles indicate shocked gas, and crosses indicate diffuse gas (as defined by the demarcation of phases in Figure 11).

Following CLWB, we parameterize the relation between rest equivalent width W_r and impact parameter r_p by a power law,

$$W_r = W_{r,0} r_p^{-\alpha}, \quad (9)$$

and determine α from linear regression using all LOS, random and selected. The fit is shown as the solid line in each panel, and the best-fit value of α is listed in the lower left. The value of $\alpha = 0.71$ does not change from $z = 1$ to $z = 0$ in the LCDM model. However, it is worth noting that the $\Omega = 1$ models, which have more late structure formation, yield $\alpha \approx 0.5$ at $z = 1$ increasing to $\alpha \approx 0.6$ at $z = 0$. The lack of significant redshift evolution of α is consistent with the results of CLWB.

CLWB find $\alpha = 0.93 \pm 0.13$ for absorbers spanning $0.1 \lesssim z \lesssim 0.8$. This slope is slightly higher than that inferred from our simulations, but within 2σ . Differences in selection procedure, spectral resolution, and other observational and numerical details could affect a precise comparison of the data with our models. For instance, numerical smoothing near a galaxy and unresolved ISM clumping inside galaxy halos both serve to lower α in our simulations. In hundreds of simulated LOS we never find an absorber with $W_r > 5\text{\AA}$, whereas CLWB found two such absorbers out of 57 (see their Table 4). Removing just these two absorbers from their sample lowers their α to 0.86,

⁴ Our results do not change significantly if we expand our velocity interval.

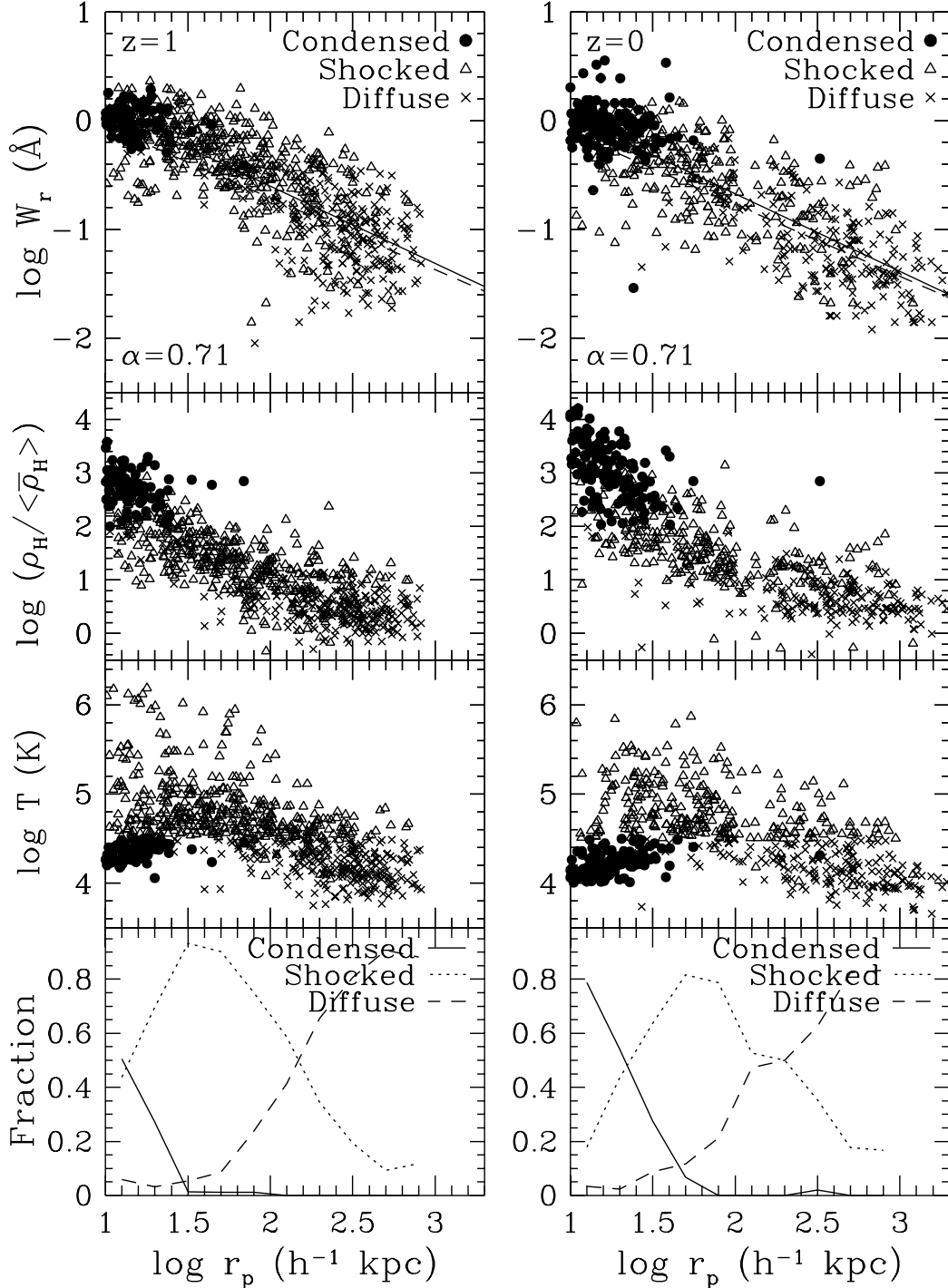


Fig. 18.— Equivalent width and physical properties of absorbers vs. impact parameter, for the LCDM model. *Top panels:* Scatter plot of equivalent width vs. impact parameter for 400 random LOS plus LOS selected to have $r_p < 100h^{-1}$ kpc, at $z = 1$ and $z = 0$. Solid line is best fit to all data points; value of α is shown in lower left. Dashed line is best fit to only diffuse IGM absorbers. Filled circles represent condensed absorbers, open triangles are shocked absorbers, and crosses are diffuse absorbers. *Second panels:* Overdensity at the peak of the neutral hydrogen density within 200 km s^{-1} of the galaxy redshift, vs. impact parameter. *Third panels:* Temperature at the peak of the neutral hydrogen density within 200 km s^{-1} of the galaxy redshift, vs. impact parameter. *Bottom panels:* Fraction of absorbers in different phases

so the effect can be significant. We also find $W_{r,0}$ in good agreement with CLWB. Thus, all of our models reproduce the observed trend of W_r vs. r_p reasonably well.

To investigate the origin of the $W_r - r_p$ correlation, we separately determine α using only those absorbers arising from diffuse gas. This fit is shown as the dashed line in the upper panels of Figure 18. In all cases, the diffuse absorber slope and overall slope are statistically indistinguishable. This shows that the observed correlation between equivalent width and impact parameter can arise from the general tendency of the large scale gas distribution to cluster around galaxies and does not require that the Ly α absorption arise in gaseous envelopes of individual galaxies.

We expect that the $W_r - r_p$ correlation will terminate or weaken at some large impact parameter, because eventually the statistics will be dominated by weak absorbers whose properties are essentially uncorrelated with the galaxy density. Such a lack of correlation on large scales has been seen observationally (SSP), although the statistics are poor. Unfortunately, our simulations are too small to determine the scale where this correlation ceases; we can only say it should extend out to $r_p \gtrsim 500h^{-1}$ kpc (comoving). This prediction is in agreement with the observations of TLS.

In the middle two panels of Figure 18 we examine the physical state of the gas giving rise to Ly α absorption near galaxies. The second panels show the peak gas overdensity along the LOS within 200 km s^{-1} of the nearest galaxy’s redshift, as a function of impact parameter, for the LCDM model at $z = 1$ and $z = 0$. The symbol types are the same as in the top panel. There is a steady trend towards higher density at lower impact parameters, down to the smallest r_p . At $r_p \sim 10h^{-1}$ kpc, the overdensities can approach 10^4 , which is still lower than the 10^6 overdensities at the centers of the galaxies in our simulations. This plot clarifies the physical origin of the $W_r - r_p$ correlation: absorbers near galaxies arise in denser gas and therefore have higher equivalent widths. There is no clear demarcation indicating a separation between gas in galaxies and gas in the IGM.

The third panels of Figure 18 show the gas temperatures at the peak overdensity. There is a slight trend of increasing temperature at smaller r_p because the diffuse gas exhibits the usual correlation between temperature and density (Figure 11) and the fraction of shock-heated absorbers increases close to the galaxies. At small impact parameters, a significant new population of absorbers appears, with temperatures around 10^4 K. These absorbers arise directly in the cold, dense gas of the galaxy.

The bottom panels of Figure 18 show the fraction of absorbers at each impact parameter arising from condensed, shocked and diffuse gas. Absorption from condensed gas extends to no more than $\sim 70h^{-1}$ kpc, even at $z = 0$. Further out, absorbers arise predominantly in shocked gas until $r_p \sim 200h^{-1}$ kpc, and at larger r_p diffuse absorbers dominate the population. We have also attempted to assess which absorbers are gravitationally bound to the potential well of the nearest galaxy and found that the majority of absorbers are bound within $r_p \sim 50h^{-1}$ kpc and unbound at larger r_p . There are very few bound absorbers with $r_p \gtrsim 100h^{-1}$ kpc. These trends are consistent

with Figure 14, which shows that the dark matter halos of galaxies in our simulation have bound extents at $z = 0$ that are typically $\sim 50h^{-1}$ kpc and rarely exceed $\sim 100h^{-1}$ kpc. We find similar results for other cosmological models.

LBTW found that 10 out of their 15 sample galaxies with $r_p < 160h^{-1}$ kpc showed detectable Ly α absorption with $W_r \gtrsim 0.3\text{\AA}$, whereas only 1 out of 9 galaxies with $r_p > 160h^{-1}$ kpc had corresponding Ly α absorption above this threshold. Based on this result, they argued that most galaxies have large gaseous envelopes $\sim 160h^{-1}$ kpc in extent and that these envelopes produce a significant fraction of low redshift Ly α forest absorbers. We compare the simulation results to the LBTW findings in Table 4. In the simulations, roughly $\sim 50 - 80\%$ of galaxies with $r_p \leq 160h^{-1}$ kpc have an absorber within 200 km s^{-1} with $W_r \geq 0.3\text{\AA}$, strong enough to be detected in the line sample used by LBTW. Conversely, for $r_p > 160h^{-1}$ kpc the fraction drops precipitously, to $\sim 10\%$. The coincidence statistics and $W_r - r_p$ correlations of LBTW and CLWB are well reproduced by our simulations, but extended gaseous envelopes bound to galaxies are not required to explain this agreement. We conclude that the identification of $\sim 160h^{-1}$ kpc as a typical gaseous envelope size by LBTW is primarily a result of their sample’s equivalent width detection limit of $W_r \gtrsim 0.3\text{\AA}$. Not coincidentally, the $W_r - r_p$ relation from CLWB would predict an absorber with $r_p = 160h^{-1}$ kpc to have $W_r \approx 0.3\text{\AA}$. A similar coincidence analysis would likely yield a smaller inferred “envelope” size for a higher W_r limit and a larger inferred size for a lower W_r limit.

The hypothesis that a significant fraction of Ly α absorbers reside in galaxy halos is well motivated theoretically (Bahcall & Spitzer 1969), and it is supported empirically by coincidence analyses, by measurements of positive absorber-galaxy cross-correlations, and by the observed $W_r - r_p$ correlation. However, our simulations appear to provide a good account of all of this observational evidence without invoking extended galaxy halos, and they also account naturally for the evidence that weaker Ly α absorbers remain correlated with galaxies but occur more often in low density environments. Some of the absorbers arise from condensed gas in galaxies, but these are a small fraction of the lines with $W_r \sim 0.24\text{\AA}$ (cf. Figure 13). Shocked gas absorbers with $r_p \lesssim 50h^{-1}$ kpc are frequently bound to the gravitational potential well of the nearest galaxy, but we have not found any sharp demarcation in physical properties between bound and unbound absorbers, and even the transition between shocked and diffuse absorbers that occurs at $r_p \sim 200h^{-1}$ kpc is slow and continuous. Setting aside the condensed absorbers, we can characterize our results as follows: low-redshift Ly α forest absorption arises in gas that traces the large scale structure of the underlying mass distribution, and because galaxies tend to lie in the densest parts of the surrounding IGM, there is a tendency for stronger absorbers to reside close to galaxies and for weaker absorbers to reside in lower density environments. This characterization is remarkably similar to the “second interpretation” of the Ly α forest described by TLS (section 6), which is the interpretation that these authors appear to favor as giving the best overall explanation of the observational data.

6. Discussion

We began our inquiry with a series of questions: Can cosmological simulations explain the sharp transition in the evolution of dN/dz observed at $z \sim 1.7$? Is the Ly α forest produced by the same physical structures at high and low redshift? Can simulations account for the apparent correlations of low- z Ly α forest absorbers with galaxies and large scale structure?

All of the cosmological models that we consider (LCDM, OCDM, TCDM, CHDM) give a fairly good match to the observed evolution of dN/dz ; in particular, all of them predict a transition from rapid evolution to slow evolution at $z \sim 1.7$. The ingredient crucial to this success is the HM photoionizing background history, and the primary cause of the break in dN/dz evolution is the transition from a roughly constant UV background intensity at $z > 2$ to a rapidly declining UV background intensity at $z < 2$. The decline in the photoionization rate counters the decline in the recombination rate caused by expansion of the universe, and the cancellation of the two effects leads to slow evolution. Gravitational growth of structure has a subsidiary but non-negligible effect on dN/dz evolution, reducing dN/dz as gas moves from lower density regions into collapsed structures that have smaller cross-sections for absorption. This transformation of the underlying structure has an important effect on the evolution of the equivalent width distribution, dN/dW_r , which steepens towards low redshift. Our quantitative dN/dz results and our qualitative conclusions about the factors that drive the evolution of dN/dz at low redshift are in good agreement with those of Theuns et al. (1998a) and, to a lesser extent, with those of Riediger et al. (1998).

The answer to the second question — is the Ly α forest produced by similar structures at high and low redshift — is a more complicated “yes and no.” At any redshift, the population of structures producing Ly α forest absorption is physically diverse, a point emphasized by Hernquist et al. (1996). The physical properties of an absorber are strongly correlated with its overdensity, and at any given redshift the overdensity is in turn correlated with the absorber’s defining observable property, its neutral column density, N_{HI} . However, the correlation between column density and overdensity changes as the universe expands (Figure 10, equation [7]), so that an absorber with a specified N_{HI} at $z = 0$ is physically analogous to an absorber with column density 20 – 50 times higher at $z = 2 - 3$. Structure formation drives a gradual migration of gas from low density regions into collapsed objects (Figure 12), but taken as a whole the population of Ly α forest absorbers is still physically similar at high and low redshift. However, the character of absorbers at a particular value of N_{HI} changes substantially between high and low redshift because a fixed column density threshold selects systems of different overdensity at different redshifts (Figure 13).

The shift in the mapping between column density and overdensity is also crucial to understanding the correlation between the Ly α forest and galaxies at low redshift. Although we do not find any indication of a significant population of lines produced by galaxy halos as opposed to lines arising in the more general large scale distribution of shocked gas, we do find

that (unsurprisingly) galaxies tend to lie in the densest regions of the surrounding IGM. At $z = 0 - 1$, the lines with column densities $N_{\text{HI}} \gtrsim 10^{14} \text{cm}^{-2}$ (typical of the large Key Project samples) arise in gas that is overdense by a factor of 20 or more, and these lines tend to occur close to galaxies. At $z = 3$, gas of this overdensity would produce lines with $N_{\text{HI}} \sim 10^{16} \text{cm}^{-2}$, approaching the column density of Lyman limit systems, which are also closely correlated with the galaxy distribution (Katz et al. 1996b, figure 2). The moderate overdensity IGM fluctuations that produce $N_{\text{HI}} \sim 10^{14} \text{cm}^{-2}$ lines at $z = 2 - 3$ produce lines with $N_{\text{HI}} \lesssim 10^{13} \text{cm}^{-2}$ at $z = 0$. Current observational evidence suggests that these lines are more smoothly distributed than stronger lines, as the simulations predict.

A power law distribution of column densities has no characteristic value, but the interplay between this distribution and the curve of growth (the relation between W_r and N_{HI}) gives a “preferred” status to marginally saturated lines, which for typical b -parameters have⁵ $N_{\text{HI}} \sim 10^{14} \text{cm}^{-2}$. Lines near this column density dominate the overall opacity of the Ly α forest, in the sense that they contribute the most opacity per logarithmic interval of N_{HI} . The fully saturated, higher column density lines are less numerous and have only slightly larger equivalent widths, while the smaller opacity of the lower column density lines is not fully compensated by their larger numbers (for a power law index $\beta > 1$). Perhaps the most significant single difference between the high- z Ly α forest and the low- z Ly α forest is that at $z > 2$ the “dominant” lines are produced mainly by unshocked gas in moderate overdensity structures (typical $\delta_H < 10$) while at $z < 1$ they are produced by shocked gas in higher overdensity regions (typical $\delta_H \sim 10 - 100$).

To recap our basic results, the simulations successfully explain the following observed properties of the low- z Ly α forest:

1. The break in the evolution of dN/dz at $z \sim 1.7$ (W98; see Figure 3).
2. The dependence of the evolution index γ on equivalent width (W98; see Figure 9).
3. The high abundance of weak ($W_r \lesssim 0.1 \text{\AA}$) lines detected in high-sensitivity spectra (TLS; a simple extrapolation from Figure 8 suggests that the simulations may predict too many weak lines).
4. The slope, amplitude, and spatial extent of the correlation between equivalent width and galaxy impact parameter (LBTW; CLWB; TLS; see Figure 18).
5. The fractions of galaxies with impact parameters $r_p < 160h^{-1} \text{ kpc}$ and $r_p > 160h^{-1} \text{ kpc}$ that have absorbers of equivalent width $W_r > 0.3 \text{\AA}$ along the line of sight (LBTW; see Table 4).
6. A variety of evidence suggesting that strong Ly α absorbers are tightly correlated with galaxies but that weaker absorbers arise preferentially in lower density environments and

⁵More precisely, the central optical depth of a Voigt-profile line is $\tau_c = 2.52(N_{\text{HI}}/10^{14} \text{cm}^{-2})(30 \text{ km s}^{-1}/b)$.

occasionally in galaxy voids (Morris et al. 1993; LBTW; Stocke et al. 1995; Le Brun et al. 1996; SSP; van Gorkom et al. 1996; Bowen et al. 1998; Lanzetta et al. 1998; Le Brun & Bergeron 1998; Grogin & Geller 1998; TLS).

The agreement between the simulations and the observational data is not always precise, and more closely matched analyses and comparisons to high-sensitivity data may show that some of the currently suggestive quantitative discrepancies are significant, at least in some of the cosmological models. Nonetheless, the qualitative success indicated by this list is remarkable because the only adjustable parameter in our modeling is the overall intensity scaling of the UV background. Furthermore, we set the value of this parameter by matching the observed Ly α flux decrement at *high* redshift, $z = 3$, leaving all of the *low- z* Ly α forest results as entirely independent predictions. The cosmological models themselves contain free parameters (Ω , h , etc.), but the values of these are set by independent cosmological considerations that have no obvious connection to the low- z Ly α forest. Although our current results do not give much handle for distinguishing among CDM models, we view the overall success of the simulations in reproducing the observed properties of the low- z Ly α forest as strong new support for the general features of the CDM scenario.

The physical model of the low- z forest that the simulations provide is difficult to summarize concisely, because the absorber population is diverse and the properties of the absorbers vary systematically with column density and with environment. In addition to the quantitative predictions described above, which can certainly be tested in greater detail than we have done here, this model makes two key predictions that can be used to test its basic validity, and perhaps to distinguish it from competing models that attribute a large fraction of the low- z forest to pressure-supported gas in mini-halos (Rees 1986; Ikeuchi 1986; Mo & Morris 1994) or to low mass clouds produced by thermal instability in galactic halos (see Mo & Miralda-Escudé 1996, who discuss this a model for Lyman limit systems).

The first prediction is that the UV background intensity decreases at low redshift, in roughly the fashion illustrated in Figure 4. The required decline in J_ν is, within current uncertainties, consistent with the predictions of HM and FGS, but those predictions assume that there are no UV background sources other than quasars, or at least that the emissivity of any additional sources tracks the emissivity of the quasar population. If we assumed a constant UV background intensity from $z = 2$ to $z = 0$, then the simulation predictions would change radically, and most of the successes cited above would vanish. Convincing evidence for a high J_ν at low redshift (i.e., similar J_ν at $z = 0$ and $z = 2$) would therefore be fatal to the physical picture that we have described. Unfortunately, direct determinations of J_ν at low redshift are far too uncertain to test this prediction at present (see Figure 4), and dramatically improving the precision of these measurements may prove difficult. The most promising route is probably to tighten the proximity effect measurement (Kulkarni & Fall 1993) using more extensive data. In the absence of such determinations, one might choose to view the success of this scenario of the low- z Ly α forest as evidence that J_ν declines at $z < 2$ and that the UV background comes largely from quasars even at $z = 0 - 1$ (though within current uncertainties our models leave room for a $\sim 50\%$ contribution

from star-forming galaxies).

The second basic prediction of our scenario is a large coherence scale for low- z Ly α forest absorbers, which can be tested by absorption studies in pairs of quasars with small angular separation. In our simulations, most Ly α forest absorption arises in systems that have low physical densities ($n_H \sim 10^{-7} \text{cm}^{-3} - 10^{-5} \text{cm}^{-3}$ for $N_{\text{HI}} \sim 10^{13} - 10^{15} \text{cm}^{-2}$) and low neutral fractions. These systems must have large path lengths in order to build up detectable neutral column densities. Models that invoke denser gas in mini-halos or pressure-confined clouds would typically predict much smaller sizes for individual absorbers. We reserve detailed predictions for future work, but it is evident from Figures 2 and 6 that absorption with $N_{\text{HI}} \sim 10^{13} - 10^{15} \text{cm}^{-2}$ should show substantial coherence across lines of sight separated by as much as several hundred h^{-1} kpc. Initial results for a quasar pair covering the absorption redshift range $0.48 < z < 0.89$ do indicate a coherence scale of hundreds of h^{-1} kpc, thus providing preliminary support for the scenario advanced here (Dinshaw et al. 1997, 1998).

Throughout this paper, we have adopted the conventional description of the Ly α forest as a collection of “lines,” each of which is produced by a distinct “absorber.” In several of our recent papers on the high-redshift Ly α forest, we have argued that it is often more profitable to view a Ly α forest spectrum as a continuous 1-dimensional map of the smoothly fluctuating IGM (e.g., Croft et al. 1997ab, 1998; Rauch et al. 1997b; Miralda-Escudé et al. 1998; Weinberg et al. 1998ab). Statistical measures that treat the transmitted flux as a continuous 1-dimensional field have two practical advantages: they do not interpose a complicated line-fitting algorithm in the path between theoretical predictions and observational data, and they can make more complete use of the information in an observed spectrum by detecting the collective signature of fluctuations that are too weak to be detected individually. At least at high redshift, the continuous IGM view also has the advantage of theoretical simplicity, because the Ly α optical depth is closely tied to the underlying mass density (Croft et al. 1997b), while the number of Ly α lines is not. This theoretical simplicity leads to analytic and numerical approximations that capture many of the basic results of full hydrodynamic simulations (Bi & Davidsen 1997; Hui et al. 1997; Croft et al. 1998; Gnedin & Hui 1998; Weinberg et al. 1998b), and these approximations can be used to obtain analytic lower bounds on the baryon density (Weinberg et al. 1997, 1998b), to span a wide range of cosmological parameters with fast numerical simulations (Gnedin 1997), to derive the power spectrum of primordial density fluctuations (Croft et al. 1998), and even to invert an observed Ly α spectrum into a line-of-sight density field (Nusser & Haehnelt 1998).

Unfortunately, it is not clear that the approximations that work well at high redshift will continue to be accurate at low redshift, since the opacity of the Ly α forest at low redshift is contributed mainly by shocked gas rather than the unshocked gas that dominates the opacity at high redshift. Shock heating introduces scatter into the relation between density and temperature (see Figure 11), and it therefore loosens the correlation between the Ly α optical depth and the underlying gas density. The practical advantages of the continuous field statistics still hold at low redshift, and we suspect that such statistics will be the most powerful tools for testing cosmological

models against Ly α forest data at all redshifts. However, the validity of techniques that have been shown to work at high redshift must be tested anew against hydrodynamic simulations at low redshift, and in many cases the accuracy of these techniques is likely to decline. We will return to these issues in future work.

There are many other opportunities for comparing these cosmological simulations to data on the low-redshift Ly α forest, including studies of metal-line absorption to constrain the enrichment and ionization state of different phases of the IGM (as pursued at high redshift by Haehnelt, Steinmetz, & Rauch 1996; Hellsten et al. 1997; Rauch, Haehnelt, & Steinmetz 1997a; Davé et al. 1998), the above-mentioned studies of absorption along paired lines of sight (see Charlton et al. 1997), studies of the evolution of Lyman limit and damped Ly α systems (pursued at high redshift by Katz et al. 1996b; Gardner et al. 1997ab; Haehnelt, Steinmetz, & Rauch 1998; Ma et al. 1997), further studies of the relationship between the absorbers and galaxies (i.e. larger volume analogs of the simulations of Katz, Hernquist & Weinberg 1992; Hernquist, Katz & Weinberg 1995; Weinberg, Hernquist & Katz 1997; Katz, Hernquist & Weinberg 1998), and studies of X-ray absorption features that can probe higher temperature gas (Cen & Ostriker 1998; Hellsten, Gnedin, & Miralda-Escudé 1998; Perna & Loeb 1998). The rapid development of computing technology and algorithms offers the prospect of larger volume, higher resolution simulations of the Ly α forest in the near future. The comparison of existing and future simulations to the increasingly detailed and sensitive observations of the high- and low-redshift Ly α forest will fulfill the original promise of quasar absorption line studies, to place firm constraints on cosmological parameters and to provide a comprehensive view of structure formation and evolution from the epoch of primeval galaxy formation to the present.

We thank J. Bahcall, B. Jannuzi, and R. Weymann for stimulating discussions, and for advance notification of their latest results. We also thank J. Miralda-Escudé for helpful comments. We are grateful to F. Haardt and P. Madau for providing us with their ionizing background in electronic form and for helpful exchanges about UV background evolution. This work was supported in part by the PSC, NCSA, and SDSC supercomputing centers, by NASA theory grants NAGW-2422, NAGW-2523, NAG5-3111, NAG5-3820, NAG5-3922, and NAG5-7047 by NASA LTSA grant NAG5-3525, and by the NSF under grants AST90-18256, ASC 93-18185, and AST 98-02568.

Table 1. Cosmological parameters for the simulations.

Model	Ω	Ω_Λ	Ω_ν	n	Ω_b	H_0	σ_8	Age ^a
LCDM	0.4	0.6	0.0	0.95	0.0473	65	0.80	14.5
TCDM	1.0	0.0	0.0	0.8	0.08	50	0.51	13.0
CHDM	1.0	0.0	0.2	1.0	0.075	50	0.70	13.0
OCDM	0.5	0.0	0.0	1.0	0.0556	60	0.72	12.7

^aIn Gyr.

Table 2. Computational and analysis parameters for the simulations.

Model	z_{start}	$m_{\text{gas}}^{\text{a}}$	$m_{\text{dark}}^{\text{a}}$	N_{steps}	$t_{\text{CPU}}^{\text{b}}$	f_{J_ν}
LCDM	49	1.06	7.9	48800	17615	1.34
TCDM	49	2.33	26.8	27656	7221	1.41
CHDM	29	2.18	21.1 ^c	15080	6845	1.50
OCDM	99	1.06	7.9	30000	— ^d	1.77

^aIn units of $10^8 M_\odot$.

^bIn Cray T3E node-hours.

^cMass of neutrino particles is $2.91 \times 10^8 M_\odot$.

^dRun completed on a different machine.

Table 3. Values of γ from observations and our four cosmological simulations.

z	Data	LCDM	TCDM	OCDM	CHDM
3 – 2	2.78 ± 0.71	2.79	4.01	2.42	3.72
2 – 1.5	unmeasured	1.35	0.90	1.25	0.42
1.5 – 0	0.26 ± 0.22	0.91	0.70	0.62	-0.17

Table 4. Fraction of galaxies with absorbers of $W_r > 0.3\text{\AA}$.

z	$r_p < 160 h^{-1} \text{ kpc}$					$r_p > 160 h^{-1} \text{ kpc}$				
	Data LBTW	LCDM	TCDM	OCDM	CHDM	Data LBTW	LCDM	TCDM	OCDM	CHDM
1	67%	76%	51%	77%	56%	11%	12%	16%	22%	17%
0	67%	65%	54%	45%	77%	11%	4%	3%	4%	12%

REFERENCES

- Bahcall, J. N., Jannuzi, B. T., Schneider, D. P., Hartig, G. F., Bohlin, R., & Junkkarinen, V. 1991, *ApJ*, 377, L5
- Bahcall, J. N., et al. 1993, *ApJS*, 87, 1
- Bahcall, J. N., et al. 1996, *ApJ*, 457, 19
- Bahcall, J. N. & Salpeter, E. E. 1965, *ApJ*, 142, 1677
- Bahcall, J. N., & Spitzer, L. 1969, *ApJ*, 156, L64
- Bechtold, J. 1994, *ApJS*, 91, 1
- Bi, H.G., 1993, *ApJ*, 405, 479
- Bi, H.G., & Davidsen, A. 1997, *ApJ*, 479, 523
- Bi, H., Ge, J., & Fang, L.-Z. 1995, *ApJ*, 452, 90
- Blumenthal, G. R., Faber, S. M., Primack, J. R., & Rees, M. J. 1984, *Nature*, 311, 517
- Bowen, D. V., Blades, J. C., & Pettini, M., 1996, *ApJ*, 464, 141
- Bowen, D. V., Pettini, M. & Boyle, B. J. 1998, *MNRAS*, 297, 239
- Bryan, G. L., Machacek, M., Anninos, P., & Norman, M. L. 1998, *ApJ*, submitted, astro-ph/9805340
- Burles, S. & Tytler, D. 1998a, *ApJ*, 499, 699
- Burles, S. & Tytler, D. 1998b, *ApJ*, submitted, astro-ph/9712109
- Carswell, R. F., Morton, D. C., Smith, M. G., Stockton, A. N., Turnshek, D. A., & Weymann, R. J. 1984, *ApJ*, 278, 486
- Cen, R., Miralda-Escudé, J., Ostriker, J.P., & Rauch M. 1994, *ApJ*, 427, L9
- Cen, R., & Ostriker, J. P. 1998, *Science*, submitted, astro-ph/9806281
- Charlton, J. C., Anninos, P., Zhang, Y., & Norman, M. L. 1997, *ApJ*, 485, 26
- Chen, H.-W., Lanzetta, K. M., Webb, J. K., & Barcons, X. 1998, *ApJ*, 498, 77 (CLWB)
- Croft, R. A. C., Weinberg, D.H., Hernquist, L., & Katz, N. 1997a, *proc. 18th Texas Symposium on Relativistic Astrophysics*, eds. A. Olinto, J. Frieman and D. Schramm, (Singapore: World Scientific), in press, astro-ph/9701166
- Croft, R. A. C., Weinberg, D. H., Katz, N., & Hernquist, L. 1997b, *ApJ*, 488, 532

- Croft, R. A. C., Weinberg, D. H., Katz, N., & Hernquist, L. 1998, *ApJ*, 495, 44
- Davé, R., Dubinski, J. & Hernquist, L. 1997a, *NewAst*, 2, 277
- Davé, R., Hellsten, U., Hernquist, L., Katz, N., & Weinberg, D. H. 1998, *ApJ*, in press, astro-ph/9803257
- Davé, R., Hernquist, L., Weinberg, D.H. & Katz, N. 1997b, *ApJ*, 477, 21
- Devriendt, J. E. G., Sethi, S. K., Guiderdoni, B., Nath, B. B. 1998, *MNRAS*, in press, astro-ph/9804086
- Dinshaw, N., Weymann, R. J., Impey, C. D., Foltz, C. B., Morris, S. L., & Ake, T. 1997, *ApJ*, 491, 45
- Dinshaw, N., Foltz, C. B., Impey, C. D., & Weymann, R. J. 1998, *ApJ*, 494, 567
- Fardal, M., Giroux, M. L., & Shull, J. M. 1998, *ApJ*, in press, astro-ph/9802246 (FGS)
- Gardner, J. P., Katz, N., Hernquist, L., & Weinberg, D. H. 1997a, *ApJ*, 484, 31
- Gardner, J. P., Katz, N., Weinberg, D. H., & Hernquist, L., 1997b, *ApJ*, 486, 42
- Gelb, J. M., & Bertschinger, E. 1994, *ApJ*, 436, 467
- Grogin, N. A., & Geller, M. J. 1998, *ApJ*, submitted, astro-ph/9804326
- Gnedin, N. Y. 1997, *MNRAS*, submitted, astro-ph/9706286
- Gnedin, N. Y., & Hui, L. 1998, *MNRAS*, 296, 44
- Gunn, J.E. & Peterson, B.A. 1965, *ApJ*, 142, 1633
- Haardt, F. & Madau, P. 1996, *ApJ*, 461, 20 (HM)
- Haehnelt, M. G., Steinmetz, M. & Rauch M. 1996, *ApJ*, 465, L95
- Haehnelt, M. G., Steinmetz, M. & Rauch M. 1998, *ApJ*, 495, 697
- Hellsten, U., Davé, R., Hernquist, L., Weinberg, D.H. & Katz, N. 1997, *ApJ*, 487, 482
- Hellsten, U., Hernquist, L., Weinberg, D.H. & Katz, N. 1998, *ApJ*, 499, 172
- Hellsten, U., Gnedin, N. Y., & Miralda-Escudé, J. 1998a, *ApJ*, submitted, astro-ph/9804038
- Hernquist, L. & Katz, N. 1989, *ApJS*, 70, 419
- Hernquist, L., Katz, N., & Weinberg, D.H. 1995, *ApJ*, 442, 57
- Hernquist, L., Katz, N., Weinberg, D.H., & Miralda-Escudé, J. 1996, *ApJ*, 457, L51

- Hu, E.M., Kim, T.S., Cowie, L.L., Songaila, A., & Rauch, M. 1995 AJ, 110, 1526
- Hui, L., & Gnedin, N. 1997, MNRAS, 292, 27
- Hui, L., Gnedin, N., & Zhang, Y. 1997, ApJ, 486, 599
- Ikeuchi, S. 1986, Ap & SS, 118, 509
- Jannuzi, B., Bahcall, J. N., Bergeron, J., Boksenberg, A., Hartig, G., Kirhakos, S., Sargent, W. L. W., Savage, B. D., Schneider, D. P., Turnshek, D. A., Weymann, R. J. & Wolfe, A. M. 1998, ApJS, 118, in press, astro-ph/9805148
- Katz, N. & Quinn, T. 1995, TIPSYS manual, <http://www-hpcc.astro.washington.edu/tools/TIPSYS>
- Katz, N., Hernquist, L., & Weinberg D.H. 1992, ApJ, 399, L109
- Katz, N., Hernquist, L., & Weinberg D.H. 1998, ApJ, submitted, astro-ph/9806257
- Katz, N., Weinberg D.H., & Hernquist, L. 1996, ApJS, 105, 19 (KWH)
- Katz, N., Weinberg D.H., Hernquist, L., & Miralda-Escudé, J. 1996b, ApJ, 457, L57
- Kim, T.S., Hu, E.M., Cowie, L.L., & Songaila, A. 1997 AJ, 114, 1 (KHCS)
- Kirkman, D. & Tytler, D. 1998, ApJ, in press, astro-ph/9701209
- Klypin, A., Nolthenius, R. & Primack, J. 1997, ApJ, 474, 533
- Klypin, A. & Holtzman, J. 1997, astro-ph/9712217
- Korista, K., Baldwin, J., & Ferland, G. 1998, ApJ, in press, astro-ph/9805338
- Kulkarni, V. P. & Fall, S. M. 1993, ApJ, 413, 63
- Kulkarni, V. P., Huang, K., Green, R. F., Bechtold, J., Welty, D. & York, D. G. 1996, MNRAS, 279, 197
- Lanzetta, K. M., Bowen, D. B., Tytler, D. & Webb, J. K. 1995, ApJ, 442, 538 (LBTW)
- Lanzetta, K. M., Webb, J. K., & Barcons, X. 1998, in Proc. of the 13th IAP Colloquium, Structure and Evolution of the IGM from QSO Absorption Line Systems, eds. P. Petitjean & S. Charlot, (Paris: Editions Frontières), in press, astro-ph/9709168
- Le Brun, V., Bergeron, J. & Boissé, P. 1996, A&A, 306, 691
- Le Brun, V. & Bergeron, J. 1998, A&A, 332, 814
- Liddle, A. R., Lyth, D. H., Roberts, D., & Viana, P. T. P. 1996a, MNRAS, 278, 644
- Liddle, A. R., Lyth, D. H., Viana, P. T. P., & White, M. 1996b, MNRAS, 282, 281

- Linder, S. M. 1998, *ApJ*, 495, 637
- Lu, L., Wolfe, A. M., & Turnshek, D. A. 1991, *ApJ*, 367, L19
- Lu, L., Sargent, W.L.W., Barlow, T.A., Churchill, C.W., & Vogt, S.S. 1996, *ApJ*, 472, 509
- Lynds, R. 1971, *ApJ*, 164, L73
- Ma, C.-P., Bertschinger, E., Hernquist, L., Weinberg, D.H., & Katz, N. 1997, *ApJ*, 484, L1
- Miralda-Escudé, J., Cen, R., Ostriker, J.P., & Rauch, M. 1996, *ApJ*, 471, 582
- Miralda-Escudé, J., Rauch, M., Sargent, W.L.W., Barlow, T.A., Weinberg, D. H., Hernquist, L., Katz, N., Cen, R., & Ostriker, J. P. 1998, in “Structure and Evolution of the IGM from QSO Absorption Line Systems”, *Proc. 13th IAP Colloquium*, eds. P. Petitjean and S. Charlot, (Paris: Editions Frontières), in press, astro-ph/9710230
- Mo, H. J., & Miralda-Escudé, J. 1996, *ApJ*, 469, 589
- Mo, H. J. & Morris, S. L. 1994, *MNRAS*, 269, 52
- Morris, S. L., Weymann, R. J., Savage, B. D., & Gilliland, R. L. 1991, *ApJ*, 377, L21
- Morris, S. L., Weymann, R. J., Dressler, A., McCarthy, P. J., Smith, B. A., Terrile, R. J., Giovanelli, R. & Irwin, M. 1993, *ApJ*, 419, 524
- Mücket, J. P., Petitjean, P., Kates, R. E., & Riediger, R. 1996, *A&A*, 308, 17
- Murdoch, H. S., Hunstead, R. W., Pettini, M., & Blades, J. C. 1986, *ApJ*, 309, 19
- Nusser, A., & Haehnelt, M. 1998, *MNRAS*, submitted, astro-ph/9806109
- Peebles, P. J. E. 1982, *ApJ*, 263, L1
- Pei, Y.-C. 1995, *ApJ*, 438, 623
- Perna, R., & Loeb, A. 1998, *ApJ*, submitted, astro-ph/9804076
- Petitjean, P., Webb, J. K., Rauch, M., Carswell, R. F., & Lanzetta, K. M. 1993, *MNRAS*, 262, 499
- Press, W.H., Rybicki, G.B., & Schneider, D.P. 1993, *ApJ*, 414, 64
- Rauch, M., Haehnelt, M. G., & Steinmetz, M. 1997a, *ApJ*, 481, 601
- Rauch, M., Miralda-Escudé, J., Sargent, W.L.W., Barlow, T.A., Weinberg D.H., Hernquist, L., Katz, N., Cen, R., & Ostriker, J.P. 1997b, *ApJ*, 489, 7
- Rauch, M., Weymann, R. J., & Morris, S. L. 1996, *ApJ*, 458, 518
- Rees, M. J. 1986, *MNRAS*, 218, L25

- Riediger, R., Petitjean, P., & Mucket, J. P. 1998, *A&A*, 329, 30
- Sargent, W.L.W., Young, P.J., Boksenberg, A., & Tytler, D. 1980, *ApJS*, 42, 41
- Scheuer, P. A. G. 1965, *Nature*, 207, 963
- Shull, J. M., Stocke, J. T., & Penton, S. 1996, *AJ*, 111, 72 (SSP)
- Stengler-Larrea, E. A., Boksenberg, A., Steidel, C. C., Sargent, W. L. W., Bahcall, J. N., Bergeron, J., Hartig, G. F., Jannuzi, B. T., Kirhakos, S., Savage, B. D., Schneider, D. P., Turnshek, D. A., Weymann, R. J. 1995, *ApJ*, 444, 64
- Stocke, J. T., Shull, J. M., Penton, S., Donahue, M. & Carilli, C. L. 1995, *ApJ*, 451, 24
- Theuns, T., Leonard, A., & Efstathiou, G. 1998a, *MNRAS*, submitted, astro-ph/9803245
- Theuns, T., Leonard, A., Efstathiou, G., Pearce, F. R., & Thomas, P. A. 1998b, *MNRAS*, submitted, astro-ph/9805119
- Tripp, T. M., Lu, L., & Savage, B. D. 1998, *ApJ*, in press, astro-ph/9806036 (TLS)
- Ulmer, A. 1996, *ApJ*, 473, 110
- van Gorkom, J. H., Carilli, C. L., Stocke, J. T., Perlman, E. S. & Shull, J. M. 1996, *AJ*, 112, 1397
- Vogel, S., Weymann, R., Rauch, M., & Hamilton, T. 1995, *ApJ*, 441, 162
- Vogt, S. S., et al. 1994, *SPIE*, 2198, 326
- Wadsley, J. W., & Bond, J.R. 1997, in *Proc. 12th Kingston Conference, Computational Astrophysics*, eds. D. Clarke & M. West, ASP Conference Series 123, (San Francisco: ASP), astro-ph/9612148
- Weinberg, D.H., Hernquist, L., & Katz, N. 1997, *ApJ*, 477, 8
- Weinberg, D.H., Hernquist, L., Katz, N., Croft, R. & Miralda-Escudé, J. 1998a, in *Proc. of the 13th IAP Colloquium, Structure and Evolution of the IGM from QSO Absorption Line Systems*, eds. P. Petitjean & S. Charlot, (Paris: Editions Frontières), astro-ph/9709303
- Weinberg, D. H., Katz, N., & Hernquist, L. 1998b, in *Origins*, eds. J. M. Shull, C. E. Woodward, & H. Thronson, (ASP Conference Series: San Francisco), astro-ph/9708213
- Weinberg, D.H., Miralda-Escudé, J., Hernquist, L., & Katz, N., 1997, *ApJ*, 490, 564
- Weymann, R., et al. 1998, *ApJ*, in press, astro-ph/9806123 (W98)
- White, M., Viana, P. T. P., Liddle, A. R. & Scott, D. 1996, *MNRAS*, 283, 107
- Zhang, Y., Anninos, P. & Norman, M.L. 1995, *ApJ*, 453, L57

Zheng, W., Kriss, G. A., Telfer, R. C., Grimes, J. P., & Davidsen, A. F. 1997, *ApJ*, 475, 469